Supporting Information

2M Phase Stability of WSe_2-$MoSe_2$ Alloy Nanosheets *via* Colloidal Reaction and Their Se-Rich Model Calculations

Ju Yeon Kim,[†] Jun Hyuk Choi,[†] Youn Jun Choi,[†] Junaid Ihsan,[†] Irtiqa Mishal,[†] Seo Yun Jeong,[†] Ha Eun Lee,[†] Jung Eun Ahn,[†] Seung Jo Yoo,[‡] Sang Gil Lee,[‡] In Hye Kwak ,*,[‡] Ik Seon Kwon,*,[≠] Jeunghee Park,*,[†] and Hong Seok Kang*,[§]

[†] Department of Advanced Materials Chemistry, Korea University, Sejong 339-700, Republic of Korea; *E-mail: parkjh@korea.ac.kr

[‡] Division of Scientific Instrumentation & Management, Korea Basic Science Institute, Daejeon 305-806, Republic of Korea; ihkwak318@kbsi.re.kr

[≠] Department of Energy Science & Engineering, Kunsan National University, Kunsan, Chonbuk 54150, Republic of Korea; *E-mail: iskwon@kunsan.ac.kr

[§] Department of Nano and Advanced Materials, Jeonju University, Chonju, Chonbuk 55069, Republic of Korea; *E-mail: hsk@jj.ac.kr

Note: J. Y. Kim, J. H. Choi, and Y. J. Choi equally contributed as the first author.

Contents

Experimental Section

Synthesis. Most of chemicals were purchased from Sigma-Aldrich and Alfa-Aesar Co. The TMD nanosheets were prepared using a hot injection colloidal synthetic route. The synthetic procedure was conducted using Schlenk line under Ar flow, following the four steps.

Step 1: 5 mL of oleylamine (OAm; $C_{18}H_{35}NH_2$; molecular weight (MW) = 267.493 g mol^{-1}, technical grade 70%, density = 0.813 g mL^{-1}) in a three-necked flask was degassed at 120 °C for 30 min, then the temperature was raised to 220-340 °C.

Step 2: 0.5 mmol of WCl_6 (tungsten hexachloride, MW = 396.61 g mol^{-1}, 99.99%)/$MoCl_5$ (molybdenum pentachloride, MW = 273.21 g mol^{-1}, 95%) and 0.5-2 mmol of $(PhCH_2)_2Se_2$ (dibenzyl diselenide; MW = 340.2 g mol^{-1}, 95%) were dissolved in 5 mL OAm and the mixture was kept at 70 °C for 2 h. The molar ratio of metal precursors and $(PhCH_2)_2Se_2$ was 1:1 or 1:4.

Step 3: 2 mL of precursor solution was injected into the preheated OAm with an injection rate of 0.4 mL min^{-1} for 5 min, and the mixture was stirred at 220-340 °C. Total reaction time is 1 h.

Step 4: The reaction solution was cooled down to room temperature and the black precipitate was separated by centrifugation. The product was washed with 1:1 ethanol:toluene mixed solvent for four times, and dried using an evaporator.

Characterization. The products were characterized by high-resolution scanning electron microscopy (SEM, Jeol), field-emission transmission electron microscopy (FE TEM, Libra 200 MC TEM), and high-voltage transmission electron microscopy high-voltage TEM (HV-TEM, Jeol JEM ARM 1300S, 1.25 MV). Energy-dispersive X-ray fluorescence spectroscopy (EDX) with elemental maps was measured using an Ultra Corrected Energy Filtering TEM operated at 200 kV that equipped with ZrO/W-field emitter system (Schottky emitter), EDS detector system (X-Max 80T, Oxford), and side CCD camera (ORIUS SC200D. Gatan). Fast Fourier-transform (FFT) images were generated by the inversion of the TEM images using Digital Micrograph GMS1.4 software (Gatan Inc.).

Spherical Aberration (Cs)-corrected scanning TEM (STEM) analysis was carried out using a Titan 80-300TM (FEI, The Netherlands) microscope operated at 200 kV. The STEM convergence semi-angle (α) used was ~18 mrad. The minimum and maximum acceptance semi-angles (β) were ~20 and 122 mrad, respectively. The dwell time per pixel was set to 0.7 μs for imaging. We used the low total dose and dwell time while measuring the STEM. The image was usually taken at a dose rate of 6×10^4 e-/nm2·s with a total dose of 1.8×10^5 e-/nm^2.

High-resolution X-ray diffraction (XRD) patterns were obtained using the 3D and 9B beamlines of the Pohang Light Source (PLS)-II with monochromatic radiation (λ = 1.52150 Å). XRD pattern measurements were also carried out in a Rigaku D/MAX-2500 V/PC using Cu K_α radiation (λ = 1.54056 Å). X-ray photoelectron spectroscopy (XPS) measurements were performed using the 8A1, 8A2, and 10A2 beam lines of the PLS-II. The photon energy of synchrotron radiation was calibrated using the standard sample; Au film, Au $4f_{7/2}$ peak at 84.0 eV. X-ray absorption near edge structure (XANES) measurements were performed using at the 7D, 8C, and 10C XAFS beamlines of the PLS-II. The X-ray beam was monochromated using a Si(111) double crystal, where the harmonic rejection was attained by detuning the beamline optics so that the intensity of the incident beam was reduced by 30%. For all the measurements, the slits had an opening of 0.5 mm (v) ×1 mm (h). All the measurements were performed at room temperature in transmission mode and the detectors were ionization-chamber-based. For the W L_3-edge, Mo K-edge, and Se K-edge measurements, the monochromator energies were calibrated using W foil, Mo foil, and Se powders, respectively. Data analysis was performed using the Athena and Artemis packages, which provide an interface to IFEFFIT.

Electrochemical Measurements. Experiments were carried in a three-electrode cell connected to an electrochemical analyzer (CompactStat, Ivium Technologies). HER electrocatalysis in 0.5 M H_2SO_4 or 1M KOH electrolyte was measured using a linear sweeping from 0 to -0.6 V (vs. RHE) with a scan rate of 2 mV s^{-1}. A saturated calomel electrode (SCE, KCl saturated, Pine Instrument) and Ag/AgCl electrode (saturated with 4 M KCl, Pine Co.) was used as a reference electrode at 0.5 M H_2SO_4 and 1 M KOH electrolyte, respectively. A Pt coil (with fritted glass) was used as a counter electrode. The electrolyte was purged with H_2 (ultrahigh grade purity 99.999%) during the measurement. The Pt counter electrode was encapsulated with a fritted glass tube (**Figure E1**), so that the Pt deposition on the working electrode was prevented.

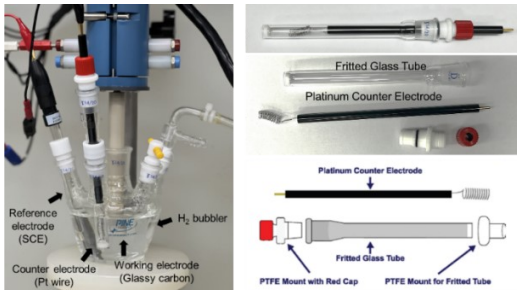

Figure E1. Photographs for our three-electrodes cell and Pt counter electrode encapsulated with a fritted glass tube, as shown on the right panel.

The applied potential (E) reported in our work was referenced to the reversible hydrogen electrode (RHE) through standard calibration as described elsewhere. We calibrate the potential of the reference electrode *vs.* standard hydrogen electrode (SHE). Cyclic voltammetry (CV) curves were obtained at a scan rate of 2 mV s^{-1}, in the high-purity H_2 saturated electrolyte with a Pt wire as the working electrode. The SCE and Ag/AgCl electrodes were used as reference electrodes for 0.5 M H_2SO_4 and 1 M KOH electrolytes, so the average value of the potential at which the current crossed at zero was -0.278 V and -0.197 V, respectively. In 0.5 M H_2SO_4, E (*vs.* RHE) = E (*vs.* SCE) + 0.278 V. In 1 M KOH, the measurements were referred to the RHE by using the relationship: E (*vs.* RHE) = E (*vs.* Ag/AgCl) + 0.197 V + 0.0592 V × pH 14 = E (*vs.* Ag/AgCl) +1.0258 V.

4 mg sample was mixed with 1 mg carbon black (Vulcan XC-72) dispersed in Nafion (20 μL) and isopropyl alcohol (0.98 mL). 32 μL catalyst ink was deposited on a glassy carbon rotating disk electrode (RDE, area = 0.1963 cm^2, Pine Instrument), making 0.652 mg cm^{-2} of catalyst materials. A rotation speed of 1600 rpm was used for the linear sweep voltammetry (LSV) measurements. The Pt/C (20 wt.% Pt in Vulcan carbon black, Sigma-Aldrich) tested as reference sample using the same procedure. The LSV curves were reproducible for four separate loadings of samples on the GC RDE electrode. For chronoamperometric stability test, we fabricated the working electrode by depositing the samples (1 mg cm^{-2}) on 1 × 1 cm^2 area of hydrophilic/waterproof carbon cloth (WIZMAC Co., thickness = 0.35 mm, through-plane resistance = 1 mΩ) that was cut with a size of 1 × 3 cm^2.

Electrochemical impedance spectroscopy (EIS) measurements were carried out for the electrode in an electrolyte by applying an AC voltage of 10 mV in the frequency range of 100 kHz to 0.1 Hz at a bias voltage of -0.15 V (vs. RHE). To measure double-layer capacitance via CV, a potential range in which no apparent Faradaic processes occur was determined from static CV. All measured current in this non-Faradaic potential region is assumed to be due to double-layer capacitance. The charging current, i_c, is then measured from CVs at multiple scan rates. The working electrode was held at each potential vertex for 10 s before beginning the next sweep. The charging current density (i_c) is equal to the product of the scan rate (ν) and the electrochemical double-layer capacitance (C_{dl}), as given by equation $i_c = \nu C_{dl}$. The difference ($\Delta J_{0.15}$) between the anodic charging and cathodic discharging currents measured at 0.15 V (*vs.* RHE) was used for i_c. Thus, a plot of $\Delta J_{0.15}$ as a function of ν yields a straight line with a slope equal to $2 \times C_{dl}$. The scan rates were 20–100 mV s^{-1}.

ECSA calculation. To estimate the actual electrochemical surface area (ECSA), we used the C_{dl} value. The roughness factor (= ECSA) is defined as the surface area ratio between the catalyst and the flat TMD electrodes. This can be obtained using $\frac{C_{dl}}{C_s}$, where C_{dl} and C_s are electrochemical double-layer capacitance of the catalysts (measured by the procedure described above) and the flat surface, respectively. The C_s value is assumed to be 0.060 mF cm^{-2} for all samples.[S1] The specific surface of the electrode can be estimated by multiplying the geometrical surface (A_{geom} = 0.1963 cm^2) to ECSA; A_{geom} × ECSA.

Table E1. ECSA of samples calculated using the equation of ECSA = C_{dl}/C_s, where C_s is the flat standard capacitor (60 μF cm^{-2}).

Electrolytes	x	C_{dl} (mF cm^{-2})	ECSA
0.5 M H_2SO_4	0	12.50	208.3
	0.25	12.95	218.8
	0.5	12.93	215.5
	0.75	13.83	230.5
	1	11.89	198.2
1 M KOH	0	12.48	208.0
	0.25	28.79	479.8
	0.5	46.36	772.7
	0.75	47.15	785.8
	1	46.75	779.2

Calculation. First-principles calculations were performed through spin-polarized density functional theory (DFT). The Vienna Ab-initio Simulation Package (VASP)[S2,S3] is mainly used for the calculations. The electron-ion interactions were described using the projector-augmented wave (PAW)[S4] method with a plane-wave kinetic energy cutoff of 400 eV. The effect of attractive van der Waals (vdW) interaction was taken into account by employing Grimme's D3 correction (PBE-D3).[S5,S6] Both ionic and lattice relaxation were performed using the PBE-D3 exchange-correlation functional and PBE+U method. When the effective Hubbard parameter (U_{eff}) was considered, U_{eff}= 2.6 eV and 3.3 eV was used for W and Mo, respectively, which are in accordance with the literature.[S7] Monkhorst-Pack *k*-point sampling of 3×3×3 was used for tgeometry optimization. Structural optimization was performed until when the total-energy change between cycles is less than 1×10^{-5} eV.

For the slab geometry, a vacuum space of 20 Å was used along the *Z* (//*c*) direction (perpendicular to the slabs) to ensure that there is no noticeable interaction between periodic

images of slabs. The Methfesser-Paxton method with a broadening of 0.2 eV is used for slabs. Total energy of a system was taken by extrapolating the smearing parameter to zero K. The convergence with respect to SCF was attained when the total-energy change between cycles is less than 1×10^{-5} eV. Monkhorst-Pack *k*-point sampling of 3×3×1 was used.

The change in Gibbs free energy during the reaction provides useful information about the energy and spontaneity of the reaction (whether it can happen without additional energy). Under standard conditions, the HER consists of two steps, the adsorption of H on the catalyst in the Volmer reaction (*), followed by the Heyrovsky/Tafel reaction to release hydrogen molecules (1/2 H_2 +*). Therefore, we should construct the Gibbs free energy profile along the reaction coordinate by calculating the relative free energies of the reactant and intermediates in the Volmer reaction. The Gibbs free energy profile along the reaction coordinate can be calculated according to the equation.[S8]

$$\Delta G = \Delta E_{DFT} + \Delta E_{ZPE} + \Delta H_{corr} - T\Delta S$$

where E_{DFT} is the total energy of hydrogen atom adsorption calculated from DFT, ΔE_{ZPE} is the zero point energy change, ΔH_{corr} is H-correction, *i.e.*, the reaction enthalpy change from 0 to 298 K, and $T\Delta S$ is the entropy change between adsorbed hydrogen and hydrogen in the gas phase under standard conditions, based on the Debye model. $H_{corr} = \int_0^{298} C_V dT$ was calculated from the vibrational heat capacity using the calculated vibrational frequencies by Harmonic Approximation.[S9] The H_2 molecule is treated as an ideal gas, while the adsorbed H is treated using the harmonic approximation. VASP calculations were used to determine the vibrational frequencies of adsorbed H atom on the system. Following **Table S0** gives each contribution to the free energy of the H_2 molecule.

Table E2. Zero-point energy correction (ΔE_{ZPE}), enthalpy correction ($\int_0^{298} C_V dT$), and entropy correction (TΔS) for gaseous H_2 molecule at the partial pressure of 1. All values are given in eV.

Species	ΔE_{ZPE}	$\int_0^{298} C_V dT$	TΔS

H_2	0.27	0.060	0.40

Table S1. Composition (mole fraction and mole ratio) of samples determined using EDX data. The mole fraction of W and Mo precursors is defined as mole fraction of corresponding precursor (WCl_6 and $MoCl_5$).

r_p	T (°C)	Precursor		Samples		
		W	Mo	W	Mo	Se/metal(%)
4	220	1	0	1	0	2.4
		0.75	0.25	0.77	0.23	2.2
		0.5	0.5	0.53	0.47	2.4
		0.25	0.75	0.30	0.70	2.2
		0	1	0	1	2.2
	260	1	0	1	0	2.3
		0.75	0.25	0.75	0.25	2.2
		0.5	0.5	0.50	0.50	2.1
		0.25	0.75	0.27	0.73	2.1
		0	1	0	1	2.1
	300	1	0	1	0	2.2
		0.75	0.25	0.71	0.29	2.2
		0.5	0.5	0.52	0.48	2.1
		0.25	0.75	0.25	0.75	2.2
		0	1	0	1	2.1
1	220	1	0	1	0	2.1
		0.75	0.25	0.73	0.27	2.1
		0.5	0.5	0.65	0.35	2.1
		0.25	0.75	0.30	0.70	2.0
		0	1	0	1	2.0
	260	1	0	1	0	2.1
		0.75	0.25	0.76	0.24	2.0
		0.5	0.5	0.57	0.43	2.0
		0.25	0.75	0.31	0.69	2.0
		0	1	0	1	2.0
	300	1	0	1	0	2.0
		0.75	0.25	0.73	0.27	2.0
		0.5	0.5	0.59	0.41	1.9
		0.25	0.75	0.33	0.67	1.8
		0	1	0	1	1.8

[Correlation of Mo and W in the samples with those of precursors]

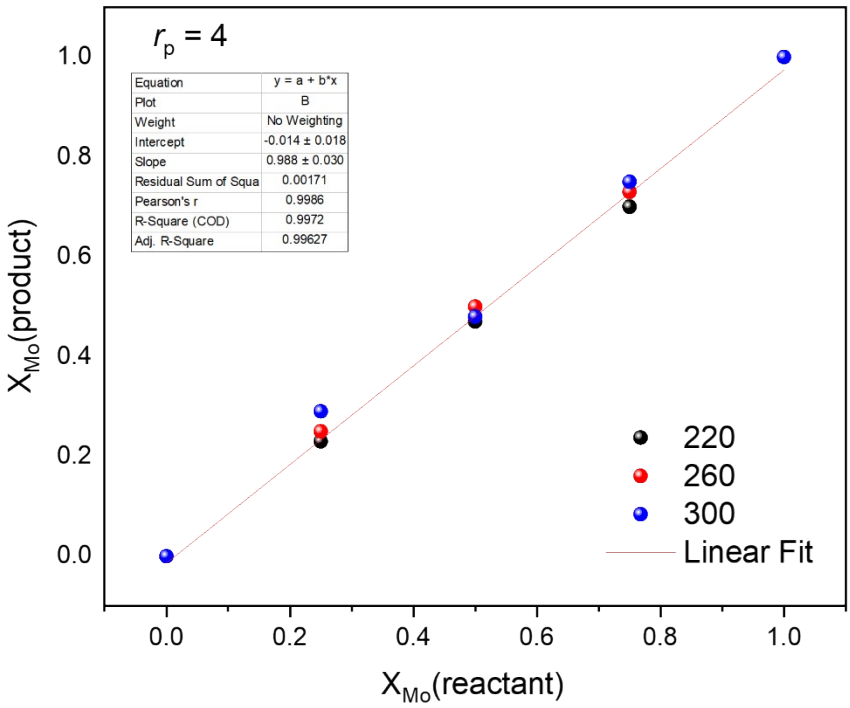
r_p = 4
Equation | y = a + b*x
Plot | B
Weight | No Weighting
Intercept | -0.014 ± 0.018
Slope | 0.988 ± 0.030
Residual Sum of Squa | 0.00171
Pearson's r | 0.9986
R-Square (COD) | 0.9972
Adj. R-Square | 0.99627
220
260
300
Linear Fit
X_{Mo}(product)
X_{Mo}(reactant)
0.0
0.2
0.4
0.6
0.8
1.0

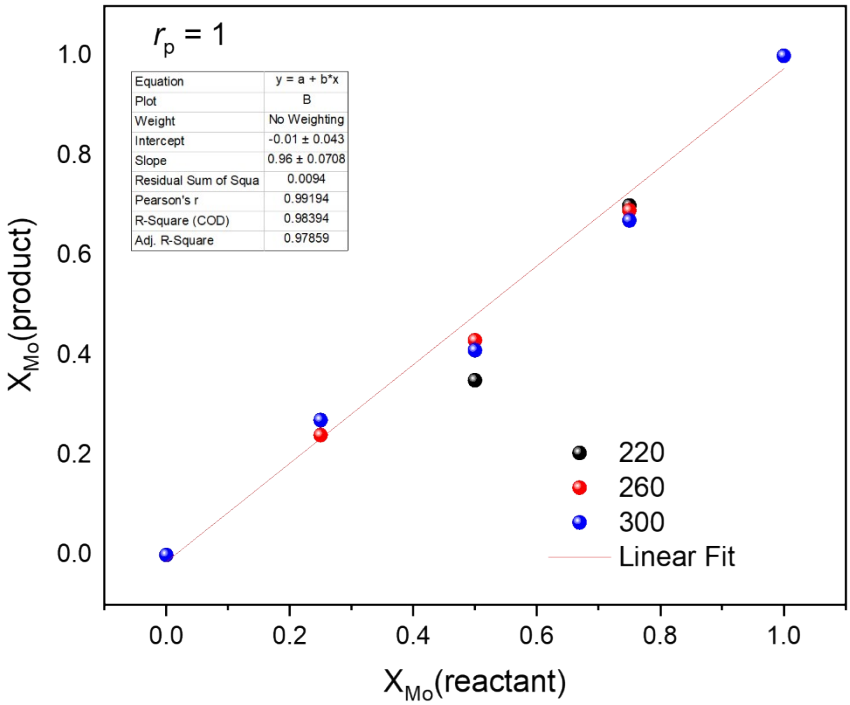
r_p = 1
Equation | y = a + b*x
Plot | B
Weight | No Weighting
Intercept | -0.01 ± 0.043
Slope | 0.96 ± 0.0708
Residual Sum of Squa | 0.0094
Pearson's r | 0.99194
R-Square (COD) | 0.98394
Adj. R-Square | 0.97859
220
260
300
Linear Fit
X_{Mo}(product)
X_{Mo}(reactant)
0.0
0.2
0.4
0.6
0.8
1.0

Table S2. Fitting parameters of EXAFS data (Figure S5) for the $W_{1-x}Mo_xSe_2$ samples with x = 0, 0.25, 0.5, 0.75, and 1) synthesized (using r_P =4) at various temperature; [a]Distance between scattering atoms, [b]Coordination number. [c]Debye-Waller factor, which measure the static and thermal disorder. [d]Edge energy shift, representing between the energy grids of experimental and theoretical data. [e]A percentage misfit between the fitted function and the data.

(a) W L_3 edge

x	Temp. (°C)	Scattering Path	R (Å)[a]	CN[b]	σ^2 (Å^2)[c]	ΔE (eV)[d]	R factor[e]
Bulk WSe_2		W-Se	2.520±0.003	6	2.57±0.12	5.13±0.79	0.005
		W-W	3.282±0.007	6	5.54±0.57		
0	220	W-Se	2.522±0.006	2.6	4.36±0.26	2.19±1.31	0.009
		W-W (2M)	2.742±0.008	2.2	4.85±0.80		
		W-W (2H)	3.203±0.030	2.0	10.7±3.00		
	260	W-Se	2.541±0.004	3.5	4.30±0.15	3.71±0.86	0.004
		W-W (2M)	2.776±0.006	2.1	4.80±0.45		
		W-W (2H)	3.267±0.004	1.7	10.5±2.87		
	340	W-Se	2.541±0.004	3.5	4.30±0.23	4.20±1.17	0.015
		W-W (2M)	2.776±0.010	2.0	4.84±0.80		
		W-W (2H)	3.267±0.018	1.6	5.54±0.20		
0.25	220	W-Se	2.532±0.010	3.5	4.29±0.19	4.02±2.17	0.005
		W-M (2M)	2.749±0.010	2.1	4.85±0.80		
		W-M (2H)	3.201±0.036	1.6	10.6±3.60		
	300	W-Se	2.535±0.006	3.9	4.32±0.21	4.60±1.42	0.006
		W-M (2M)	2.759±0.013	1.7	4.75±0.92		
		W-M (2H)	3.187±0.021	0.3	11.6±2.04		
	340	W-Se	2.535±0.006	3.9	4.24±0.20	4.73±1.22	0.005
		W-M (2M)	2.778±0.014	1.7	4.68±1.11		
		W-M (2H)	3.262±0.019	1.8	5.46±1.77		
0.5	220	W-Se	2.526±0.007	4.6	4.24±0.22	3.00±1.63	0.009
		W-M (2M)	2.727±0.015	1.7	5.06±0.88		
		W-M (2H)	3.153±0.021	1.6	10.6±4.29		
	300	W-Se	2.533±0.004	4.6	4.24±0.14	4.10±0.97	0.004
		W-M (2M)	2.773±0.012	1.2	4.62±1.04		
		W-W (2H)	3.223±0.021	1.9	11.0±3.35		
0.75	220	W-Se	2.533±0.005	5.1	5.78±0.79	3.44±0.99	0.015
		W-W (2M)	2.862±0.001	1.1	4.59±0.92		
	260	W-Se	2.528±0.009	5.0	5.04±0.33	2.42±1.41	0.011
		W-M (2M)	2.862±0.001	2.0	5.02±0.87		
		W-M (2H)	3.443±0.017	4.0	5.25±0.83		
	300	W-Se	2.530±0.006	5.8	4.27±0.22	4.55±1.51	0.011
		W-M (2M)	2.933±0.001	2.0	11.2±3.79		
		W-M (2H)	3.432±0.015	4.5	5.85±0.90		

(b) Mo K edge

x	Temp. (°C)	Scattering Path	R (Å)[a]	CN[b]	σ^2 (Å^2)[c]	ΔE (eV)[d]	R factor[e]
Bulk $MoSe_2$		Mo-Se	2.528±0.001	6	2.45±0.16	1.96±0.97	0.009
		Mo-Mo	3.301±0.001	6	6.28±0.71		
0.25	220	Mo-Se	2.528±0.006	4.8	6.11±0.22	-1.35±1.25	0.003
		Mo-M (2M)	2.891±0.014	2.0	10.8±2.80		
		Mo-M (2H)	3.263±0.001	3.0	3.52±0.71		
	260	Mo-Se	2.536±0.006	6.0	4.55±0.25	0.92±1.58	0.013
		Mo-M (2M)	2.928±0.032	2.0	10.5±3.62		
		Mo-M (2H)	3.331±0.051	0.7	5.76±4.82		
	340	Mo-Se	2.537±0.007	6.0	5.32±0.32	-0.33±1.18	0.015
		Mo-M (2H)	3.301±0.029	1.5	6.35±2.85		
0.5	220	Mo-Se	2.538±0.003	5.4	7.55±0.12	0.69±0.60	0.001
		Mo-M (2M)	2.841±0.016	1.0	11.4±1.80		
		Mo-M (2H)	3.272±0.011	0.6	5.66±1.11		
	300	Mo-Se	2.530±0.003	5.7	3.57±0.15	1.67±0.83	0.001
		Mo-M (2H)	3.294±0.011	4.7	6.31±0.62		
0.75	220	Mo-Se	2.529±0.017	5.2	7.50±0.68	-3.62±1.74	0.026
		Mo-M (2M)	2.840±0.043	2.0	8.23±2.56		
		Mo-M (2H)	3.188±0.075	0.5	6.16±0.76		
	260	Mo-Se	2.530±0.003	5.7	3.61±0.13	0.98±0.78	0.005
		Mo-M (2H)	3.292±0.009	3.2	6.40±0.79		
	300	Mo-Se	2.533±0.004	5.0	3.82±0.17	0.30±1.04	0.009
		Mo-M (2H)	3.289±0.012	2.5	6.46±1.13		
1	220	Mo-Se	2.535±0.005	6.0	6.40±0.22	-1.02±1.39	0.005
		Mo-Mo (2M)	2.822±0.024	1.5	10.8±2.80		
		Mo-Mo (2H)	3.248±0.008	1.4	3.52±0.71		
	300	Mo-Se	2.530±0.005	5.0	2.54±0.25	0.57±1.39	0.018
		Mo-Mo (2H)	3.293±0.011	5.8	6.30±0.88		

(c) Se K edge

x	Temp. (°C)	Scattering Path	R (Å)[a]	CN[b]	σ^2 (Å^2)[c]	ΔE (eV)[d]	R factor[e]
Se powder		Se-Se	2.379±0.004	2	4.32±0.43	4.58±1.04	0.004
Bulk WSe_2		Se-W	2.530±0.003	3	4.32±0.11	4.39±1.08	0.007
		Se-Se	3.305±0.007	6	7.82±0.40		
Bulk $MoSe_2$		Se-Mo	2.530±0.004	3	3.73±0.18	4.79±1.25	0.014
		Se-Se	3.301±0.08	6	8.46±0.56		
	220	Se-Se	2.391±0.011	0.3	8.98±0.84	4.47±1.58	0.009
		Se-W	2.544±0.008	1.8	8.94±0.45		

		Se-Se	3.385±0.013	5.0	18.2±1.07		
	260	Se-Se	2.364±0.019	0.3	8.73±1.67	4.79±1.25	0.006
		Se-W	2.544±0.005	1.8	6.02±0.24		
		Se-Se	3.353±0.001	5.0	14.8±0.70		
	300	Se-Se	2.384±0.015	0.2	8.98±0.84	5.24±1.08	0.003
		Se-W	2.545±0.004	1.8	8.94±0.45		
		Se-Se	3.351±0.007	5.0	18.2±1.07		
1	220	Se-Se	2.338±0.008	0.3	3.91±0.93	4.91±1.41	0.008
		Se-Mo	2.544±0.005	1.8	7.41±0.57		
		Se-Se	3.353±0.001	3.1	13.9±1.04		
	300	Se-Mo	2.525±0.003	1.6	2.89±0.10	3.33±0.86	0.008
		Se-Se	3.287±0.006	3.3	8.53±0.40		

Table S3. Parameters of two layered (4×4×1) supercells for (a) pristine, (b) pristine with U_{eff} (P^U), (c) metal vacancy (MV), and (d) metal vacancy/Se intercalation combined (MV + I) models of $W_{1-x}Mo_xSe_2$.

(a) Pristine model with U_{eff} = 0

x	Phase	a, b, c (Å)	α, β, γ (°)	d_L (Å)[a]	E_{rel} (eV)	E_{rel}/atom (meV)[b]
0	2H	13.16, 12.99	90, 90, 120	6.50	0	0
	2M	11.87, 13.17, 13.68	90, 109.66, 90	6.44	9.891	103.031
	1T′	13.58, 13.12, 13.11	90, 90, 119	6.56	10.679	111.240
0.25	2H	13.17, 13.02	90, 90, 120	6.51	0	0
	2M	11.91, 13.19, 13.69	90, 112.01, 90	6.35	9.809	102.174
	1T′	13.59, 13.11, 13.08	90, 90, 119	6.54	10.739	111.863
0.5	2H	13.18, 13.02	90, 90, 120	6.51	0	0
	2M	11.92, 13.19, 13.62	90, 112.37, 90	6.30	10.100	105.213
	1T′	13.60, 13.09, 13.02	90, 90, 119	6.51	11.040	114.998
0.75	2H	13.18, 13.02	90, 90, 120	6.51	0	0
	2M	11.94, 13.19, 13.55	90, 112.71, 90	6.25	10.407	108.405
	1T′	13.61, 13.08, 12.99	90, 90, 119	6.50	11.341	118.135
1	2H	13.18, 12.99	90, 90, 120	6.50	0	0
	2M	11.95, 13.15, 13.47	90, 113.13, 90	6.19	11.227	116.944
	1T′	13.60, 13.06, 12.98	90, 90, 119	6.49	11.867	123.615

(b) Pristine model with U_{eff} = 2.6 eV for W and U_{eff} = 3.3 eV for Mo.

x	Phase	a, b, c (Å)	α, β, γ (°)	d_L (Å)[a]	E_{rel}^{U} (eV)	E_{rel}^{U}/atom (meV)[b]
0	2H	13.22, 13.05	90, 90, 120	6.53	0	0
	2M	11.92, 13.28, 13.71	90, 109.55, 90	6.46	8.160	85.004
	1T′	13.63, 13.26, 13.07	90, 90, 119	6.54	8.831	91.985
0.25	2H	13.23, 13.05	90, 90, 120	6.53	0	0
	2M	11.92, 13.29, 13.77	90, 111.81, 90	6.39	8.020	83.546
	1T′	13.64, 13.25, 13.08	90, 90, 119	6.54	8.855	92.239
0.5	2H	13.23, 13.06	90, 90, 120	6.53	0	0
	2M	11.94, 13.29, 13.75	90, 111.91, 90	6.38	8.017	83.507
	1T′	13.64, 13.24, 13.05	90, 90, 119	6.53	8.735	90.994
0.75	2H	13.24, 13.05	90, 90, 120	6.53	0	0
	2M	11.96, 13.28, 13.69	90, 112.04, 90	6.34	8.034	83.685
	1T′	13.65, 13.23, 13.05	90, 90, 119	6.53	8.852	92.213
1	2H	13.24, 13.02	90, 90, 120	6.51	0	0
	2M	12.00, 13.32, 13.48	90, 112.79, 90	6.21	7.993	83.256
	1T′	13.67, 13.22, 12.95	90, 90, 119	6.48	8.846	92.151

(c) Metal vacancy (MV) model with U_{eff} = 0

x	Metal	Phase	a, b, c (Å)	α, β, γ (°)	d_L (Å)[a]	E_{rel} (eV)	E_{rel}/atom (meV)[b]	E_{MV} (eV)[c]
0	W	2H	13.21, 12.91	90, 90, 120	6.46	0	0	5.188
		2M	11.97, 13.19, 13.66	90, 112.39, 90	6.32	5.064	53.872	2.774
		1T′	13.66, 13.16, 12.84	90, 90, 119	6.42	6.002	63.851	2.850
0.25	W	2H	13.21, 12.85	90, 90, 120	6.43	0	0	5.067
		2M	12.21, 13.21, 13.29	90, 112.94, 90	6.12	5.656	60.171	2.991
		1T′	13.68, 13.06, 12.76	90, 90, 119	6.38	6.509	69.249	2.953
	Mo	2H	13.21, 12.91	90, 90, 120	6.46	0	0	5.400
		2M	12.01, 13.22, 13.30	90, 112.84, 90	6.13	5.624	59.829	3.307

		1T′	13.67, 13.10, 12.73	90, 90, 119	6.37	6.524	69.408	3.292
0.5	W	2H	13.21, 12.85	90, 90, 120	6.43	0	0	5.113
		2M	12.04, 13.18, 13.23	90, 113.28, 90	6.08	6.001	63.843	3.063
		1T′	13.68, 13.03, 12.76	90, 90, 119	6.38	6.901	73.417	3.043
	Mo	2H	13.21, 12.85	90, 90, 120	6.43	0	0	5.431
		2M	12.03, 13.26, 13.25	90, 113.26, 90	6.09	5.717	60.824	3.240
		1T′	13.68, 13.05, 12.74	90, 90, 119	6.37	6.863	73.009	3.343
0.75	W	2H	13.20, 12.89	90, 90, 120	6.45	0	0	5.300
		2M	12.06, 13.18, 13.17	90, 113.63, 90	6.03	6.070	64.576	3.132
		1T′	13.68, 12.98, 12.78	90, 90, 119	6.39	7.038	74.872	3.149
	Mo	2H	13.21, 12.87	90, 90, 120	6.44	0	0	5.458
		2M	12.06, 13.24, 13.19	90, 113.60, 90	6.04	6.045	64.310	3.277
		1T′	13.68, 12.99, 12.76	90, 90, 119	6.38	7.181	76.396	3.378
1	Mo	2H	13.18, 12.88	90, 90, 120	6.44	0	0	5.739
		2M	12.04, 13.21, 13.33	90, 113.54, 90	6.11	5.866	62.404	3.223
		1T′	13.71, 13.16, 12.51	90, 90, 119	6.26	6.741	71.713	3.176

(d) Metal vacancy/Se intercalation combination (MV + I) model with $U_{eff} = 0$

x	Metal	Phase	a, b, c (Å)	α, β, γ (°)	d_L (Å)[a]	E_{rel} (eV)	E_{rel} /atom (meV)[b]	E_{MV} (eV)[c]	E_I (eV)[d]
0	W	2H	13.25, 14.78	90, 90, 120	7.39	0	0	3.761	1.590
		2M	12.03, 13.28, 15.47	90, 114.11, 90	7.06	2.871	29.296	2.836	1.041
0.25	W	2H	13.26, 14.63	90, 90, 120	7.32	0	0	3.119	1.271
		2M	12.05, 13.15, 15.05	90, 113.90, 90	6.88	3.920	40.000	2.563	0.837
	Mo	2H	13.23, 14.86	90, 90, 120	7.43	0	0	3.883	1.487
		2M	12.01, 13.19, 15.11	90, 113.09, 90	6.95	3.046	31.086	2.890	0.843
0.5	W	2H	13.28, 14.89	90, 90, 120	7.45	0	0	3.038	1.169
		2M	12.03, 13.15, 15.04	90, 113.09, 90	6.92	4.543	46.357	2.622	0.804
	Mo	2H	13.28, 14.62	90, 90, 120	7.31	0	0	3.520	1.251
		2M	12.06, 13.19, 15.16	90, 114.61, 90	6.89	4.077	41.602	2.872	0.841
0.75	W	2H	13.25, 14.85	90, 90, 120	7.43	0	0	3.638	1.281
		2M	12.04, 13.07, 15.07	90, 113.17, 90	6.93	4.083	41.665	2.722	0.785
	Mo	2H	13.28, 14.58	90, 90, 120	7.29	0	0	3.588	1.178
		2M	12.08, 13.17, 15.07	90, 114.48, 90	6.86	4.494	45.857	2.878	0.790
1	Mo	2H	13.25, 14.46	90, 90, 120	7.23	0	0	3.803	1.132
		2M	12.09, 13.24, 15.24	90, 114.19, 90	6.95	4.921	50.214	3.197	0.896

[a] Interlayer distance, $d_L = ½\ c$ for 2H and 1T′, while $d_L = ½\ (c \times \sin\beta)$ for 2M.

[b] Relative energy per atom; E_{rel}/N, where $E_{rel} = E_{2M\ (or\ 1T')} - E_{2H}$ and N is the number of atoms in the supercell.

[c] Metal vacancy formation energy of metal atoms (per vacancy), defined as E_{MV} = [E (Metal vacancy model) + 2μ(M) – E (Pristine)]/2. E is the total energy of the model, and μ(metal) is the chemical potential of a metal atom in the body-centered cubic crystal. For the MV model, the metal removal reaction is $M_{32}Se_{64}$ (denoted as MSe_2)→ $M_{30}Se_{64}$ (denoted as $MSe_{2.13}$) + 2M. For the MV+I model, the reaction is $M_{32}Se_{66}$ (denoted as $MSe_{2.27}$)→ $M_{30}Se_{66}$ (denoted as $MSe_{2.13}$) + 2M.

[d] Se intercalation energy (per Se), defined as E_I = [E ($M_{30}Se_{66}$ = $MSe_{2.27}$) – E($M_{30}Se_{64}$ = $MSe_{2.13}$) - 2μ(Se)]/2 for the intercalation reaction of $M_{30}Se_{64}$+ 2Se → $M_{30}Se_{66}$, where E is the total energy of the model, *n* is the number of Se atoms, and μ(Se) is the chemical potential of a Se atom in the dimer.

Table S4. HER performance of $W_{1-x}Mo_xSe_2$ samples synthesized at 220 °C.

Electrolyte	x	$\eta_{J=10}$ (mV)[a]	b (mV dec^{-1})[b]	R_{ct} (Ω)[c]	C_{dl} (mF cm^{-2})[d]	$\eta_{JECSA=0.1}$(mV)[e]
0.5 M H_2SO_4	0	139	72	22.4	12.50	162
	0.25	130	63	12.7	12.95	150
	0.5	128	65	13.6	12.93	149
	0.75	123	66	11.1	13.83	148
	1	121	60	9.2	11.89	144
1 M KOH	0	372	152	8273	12.48	425
	0.25	330	110	336	26.79	416
	0.5	294	100	374	46.36	411
	0.75	286	101	182	47.15	403
	1	278	117	387	46.75	410

[a] Overpotential (mV *vs.* RHE) at J = 10 mA cm^{-2}; [b] Tafel slope for HER; [c] Charge transfer resistance obtained using Nyquist plot of EIS data; [d] Double layer capacitance; [e] Overpotential (mV *vs.* RHE) at J_{ECSA} = 0.1 mA cm^{-2}.

Table S5. Comparison of HER performance of (a) WX_2 samples in 0.5 M H_2SO_4 and (b) MoX_2/WX_2 samples in 1 M KOH in the literatures. If the phase of materials is not defined, it is presumably 2H.

(a)

Ref. No.	Materials	$\eta_{J=10}$ (mV)	Tafel slope (mV dec^{-1})
S10	Exfoliated 1T WS_2	250	60
S11	Exfoliated 1T phase 2% V-doped WSe_2	750	120
S12	Colloidal 1T WS_2	200	50.4
S13	Hydrothermal WO_3/sulfurization 6.5% V-doped WS_2	148	72
S14	Co:$W_{18}O_{49}$-sulfurized Co-doped WS_2	210	49
S15	1T′ phase WSe_2 (colloidal)	510	150
S16	10% Ni-doped WSe_2	259	86
S17	4% V-doped WS_2	185	61
S18	1.5 wt.% Co-doped WSe_2	140	76
S19	$CoSe_2/WSe_2$ hybrid	157	79
S20	Colloidal 1T' WSe_2	232	59
S21	1T WSe_2 on substrate by heating up method	197	143
S22	$W_{0.9}V_{0.1}Se_2$	128	80
S23	$W_{0.8}Nb_{0.2}Se_2$	125	69
S24	$W_{0.9}Mo_{0.1}Se_2$	135	69
This work	2M phase WSe_2 $W_{0.5}Mo_{0.5}Se_2$	139 128	72 65

(b)

Ref. No.	Materials	$\eta_{J=10}$ (mV)	Tafel slope (mV dec^{-1})
S25	$Ni_{0.54}W_{0.26}Se_2$ WSe_2	190 378	74 137
S26	$NiS_2/CoS_2/MoS_2$	112	59
S27	10%Ni/WSe_2 WSe_2	215 375	109 152
S28	Ni-$MoSe_2$ MoS_2	184 355	83 118
S29	Co_9S_8/MoS_2 on Ni foam MoS_2 on Ni foam	167 349	81.7 86.1
S30	$CoSe_2/MoSe_2$	168 >600	106.4 134.5

S31	$Ni_{0.85}Se/MoSe_2$ $MoSe_2$	163 108	77 87
S32	2M $Re_{0.15}W_{0.85}S_2$ WS_2	107 685	106 266
S33	$MoSe_2$ in 1M KOH+0.10 MoO_4^{2-} $MoSe_2$ in 1M KOH	337 245	156.32 107.74
S34	$NiSe/WSe_2$ WSe_2	21 208	45.2 122.9
S35	$MoP/MoSe_2$ $MoSe_2$	47 201	74 142
S36	WS_2/W-CoP_x WS_2	81 150	132 148
S37	MoS_2 WS_2	256 493.5	115 166
S38	Strained $MoSe_2$	101.1	122.4
S39	1T/2H WS_2/N-rGO WS_2	80.35 371.15	126.58 262.37
S40	$Ni_3S_2/MoS_2/WS_2$	165	77
This work	2M phase WSe_2 $W_{0.5}Mo_{0.5}Se_2$	372 294	152 101

(a)

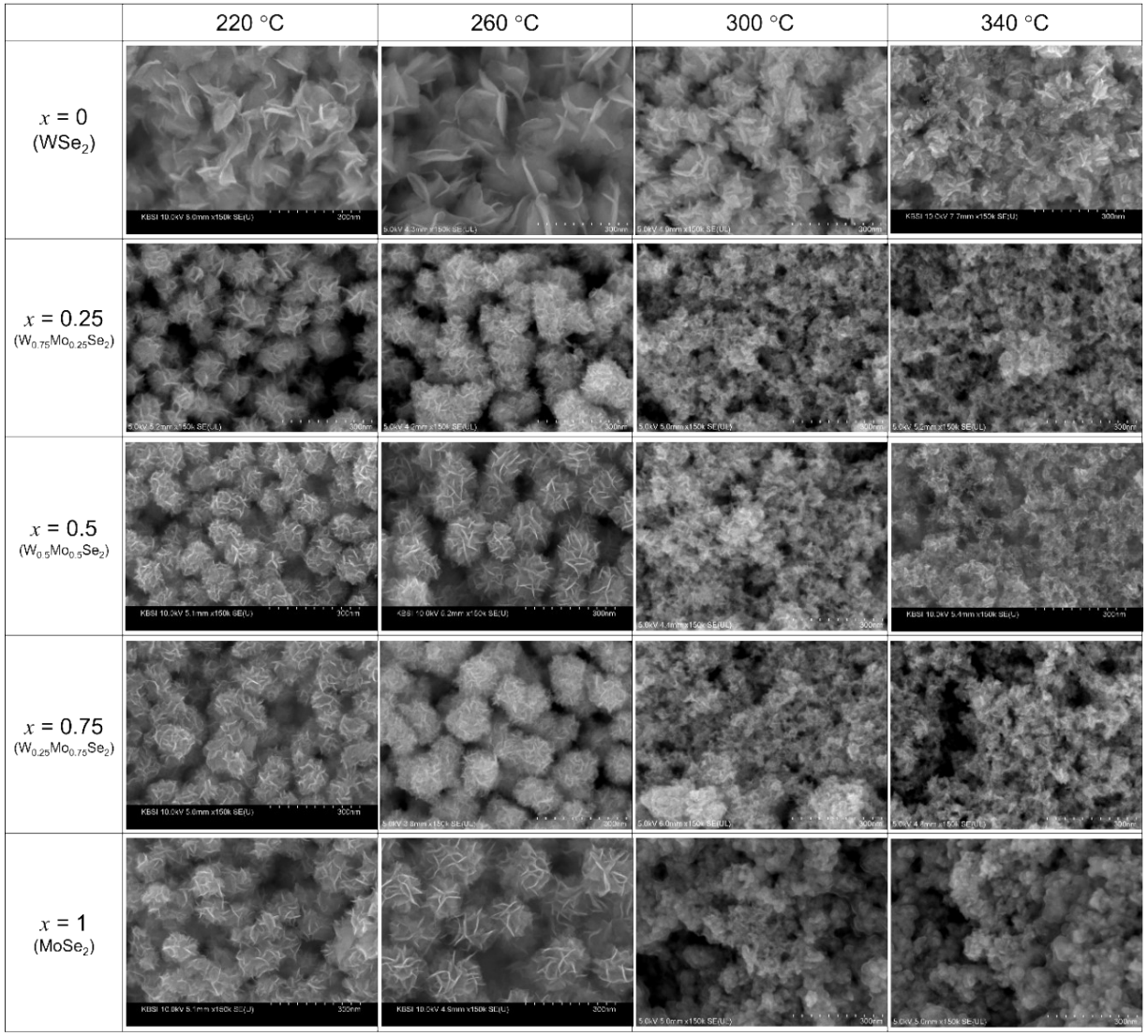
220 °C
260 °C
300 °C
340 °C
x = 0
(WSe2)
x = 0.25
(W0.75Mo0.25Se2)
x = 0.5
(W0.5Mo0.5Se2)
x = 0.75
(W0.25Mo0.75Se2)
x = 1
(MoSe2)

WSe_2

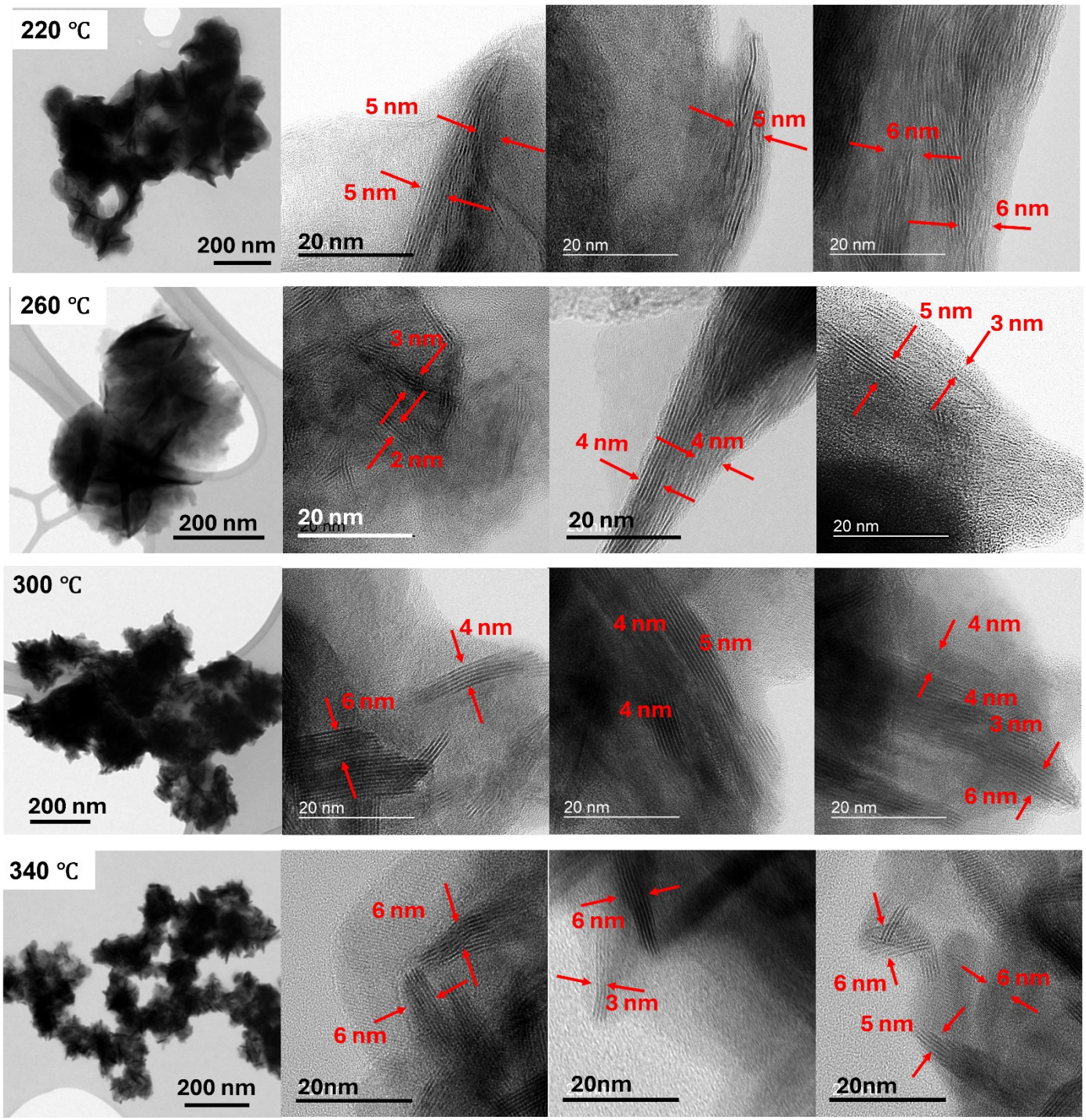
220 ℃
200 nm
5 nm
5 nm
20 nm
5 nm
20 nm
6 nm
6 nm
20 nm
260 ℃
200 nm
3 nm
2 nm
20 nm
4 nm
4 nm
20 nm
5 nm
3 nm
20 nm
300 ℃
200 nm
4 nm
6 nm
20 nm
4 nm
5 nm
4 nm
20 nm
4 nm
4 nm
3 nm
6 nm
20 nm
340 ℃
200 nm
6 nm
6 nm
20nm
6 nm
3 nm
20nm
6 nm
6 nm
5 nm
20nm

$MoSe_2$

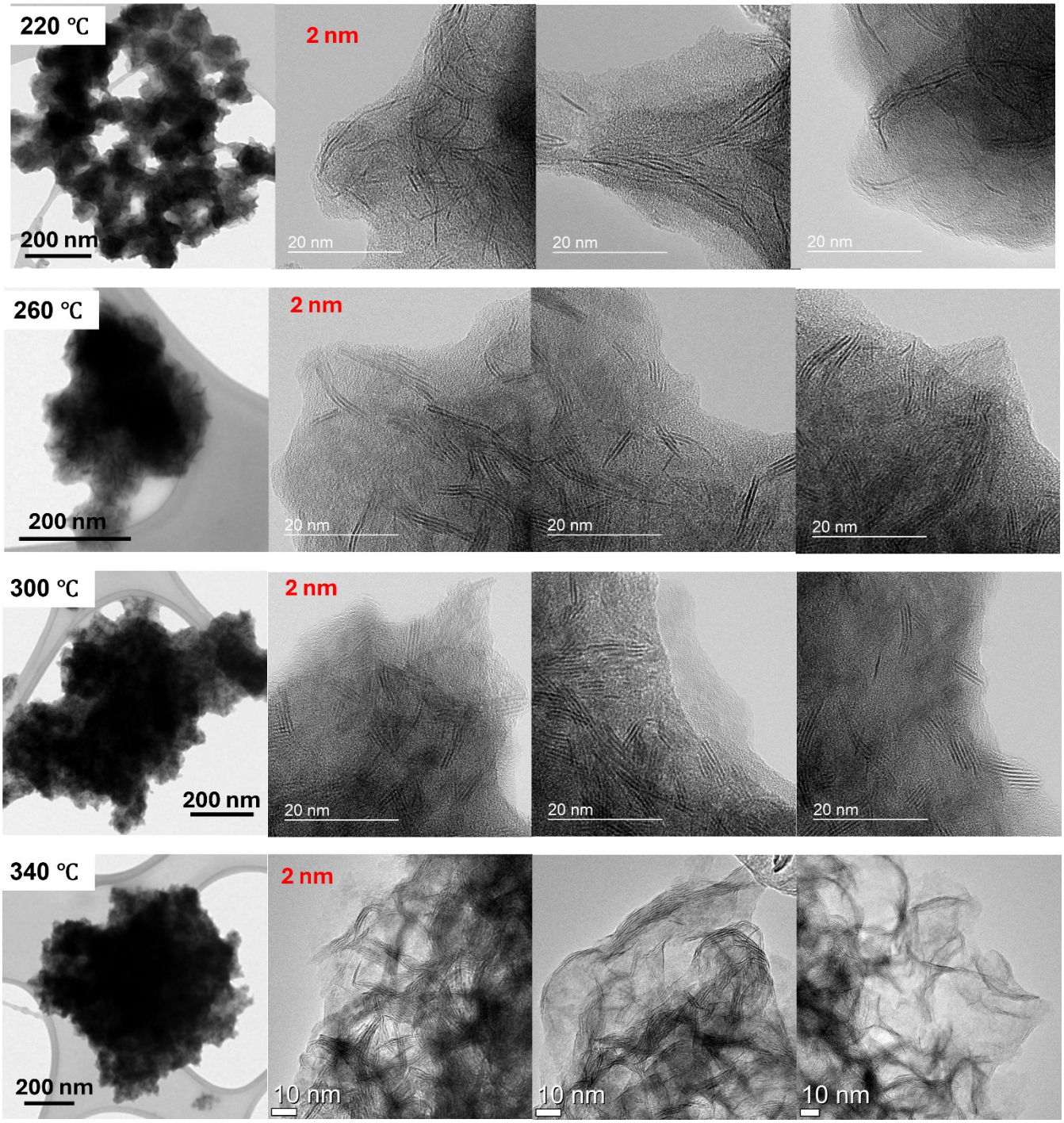
220 ℃
200 nm
2 nm
20 nm
20 nm
20 nm
260 ℃
200 nm
2 nm
20 nm
20 nm
20 nm
300 ℃
200 nm
2 nm
20 nm
20 nm
20 nm
340 ℃
200 nm
2 nm
10 nm
10 nm
10 nm

$W_{0.75}Mo_{0.25}Se_2$

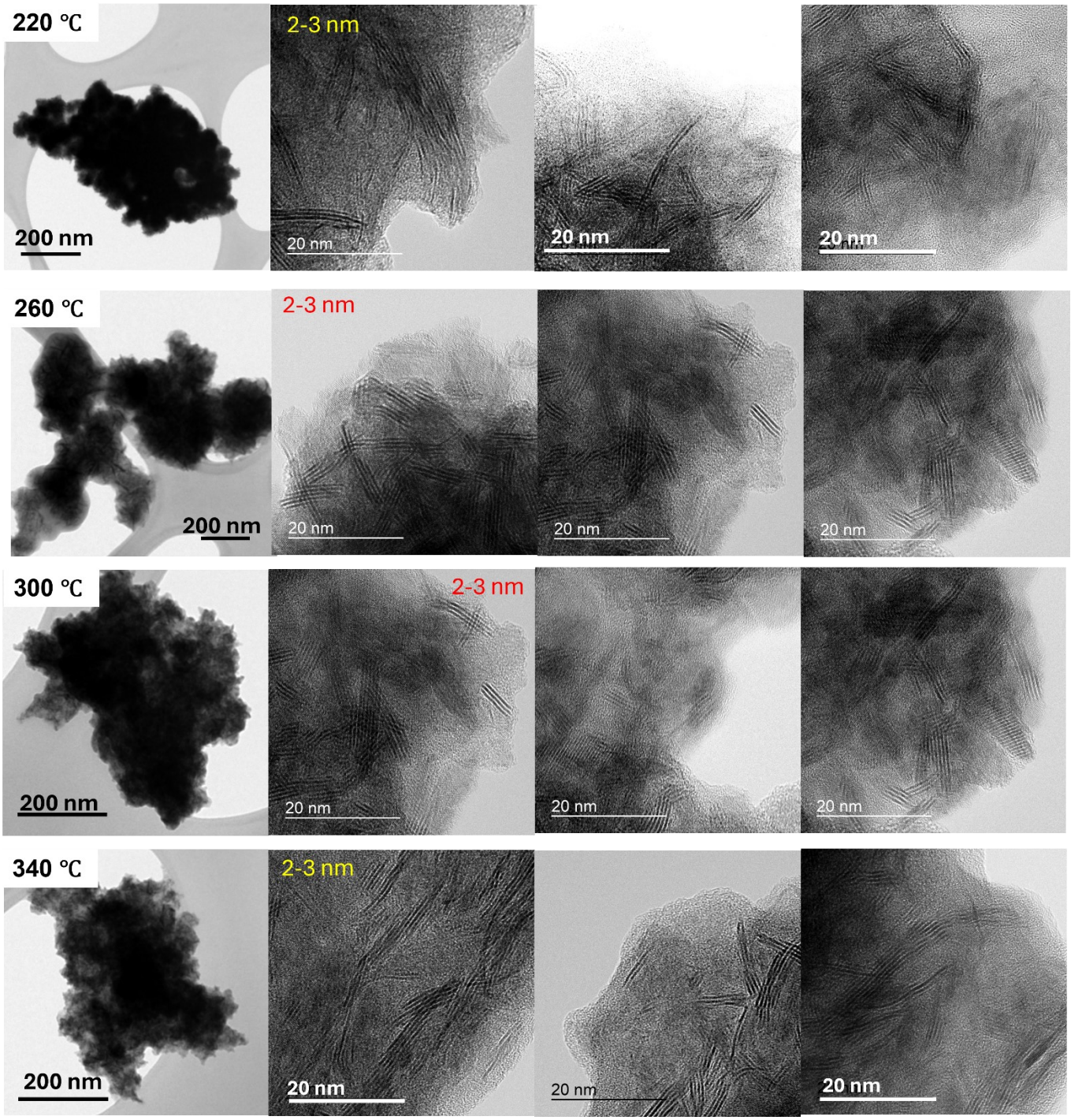

$W_{0.5}Mo_{0.5}Se_2$

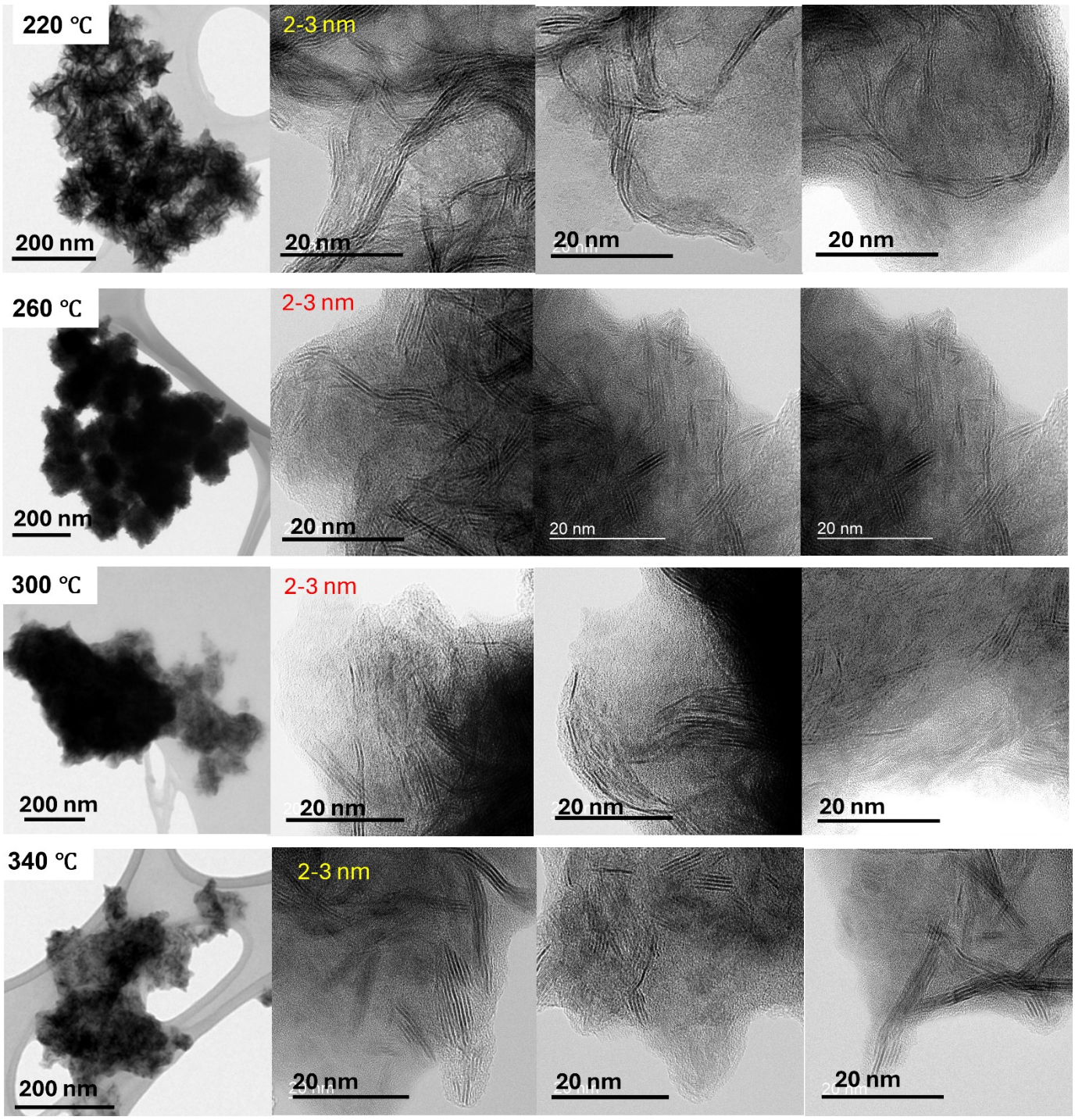
220 ℃
200 nm
2-3 nm
20 nm
20 nm
20 nm
260 ℃
200 nm
2-3 nm
20 nm
20 nm
20 nm
300 ℃
200 nm
2-3 nm
20 nm
20 nm
20 nm
340 ℃
200 nm
2-3 nm
20 nm
20 nm
20 nm

$W_{0.25}Mo_{0.75}Se_2$

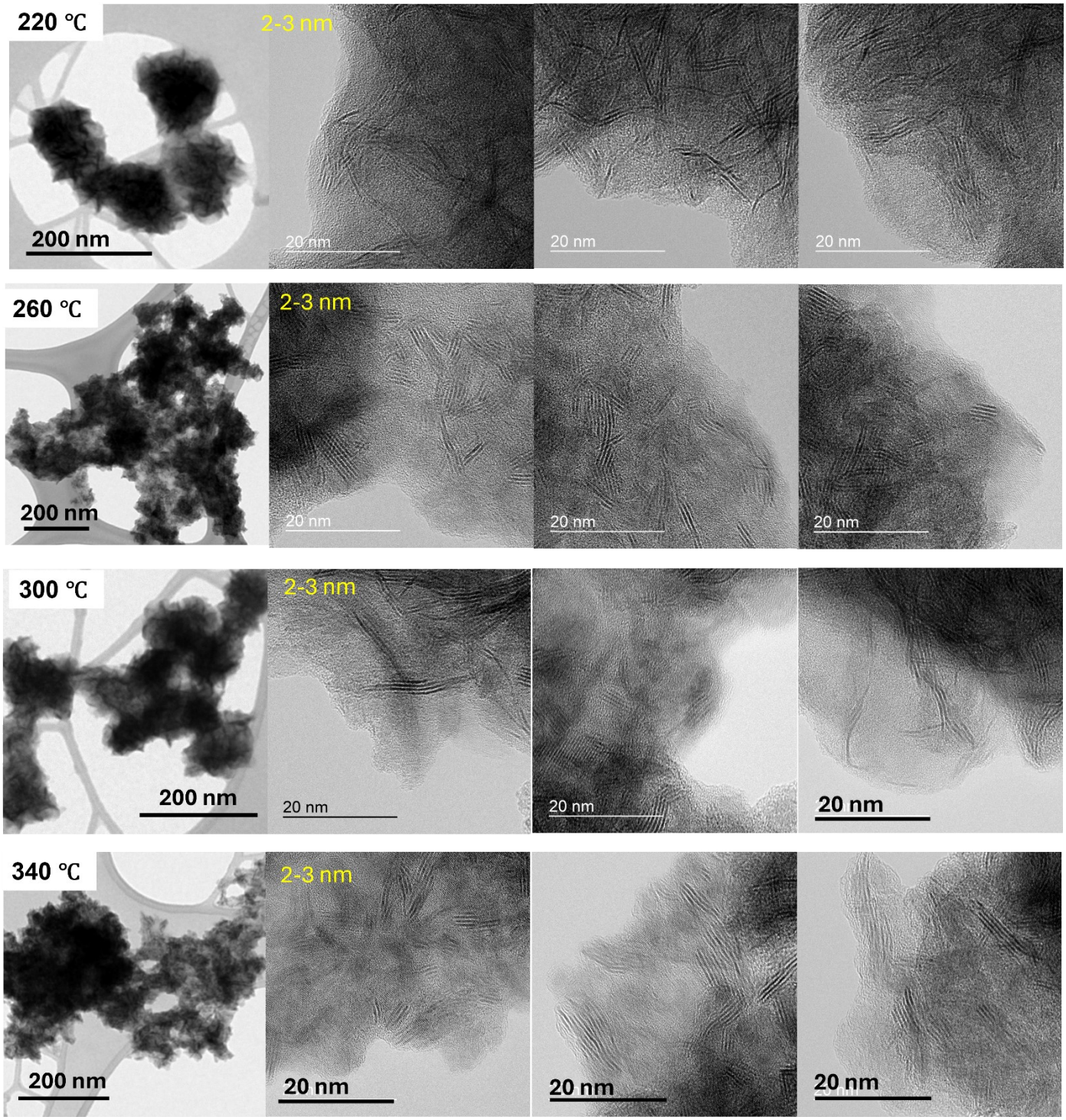

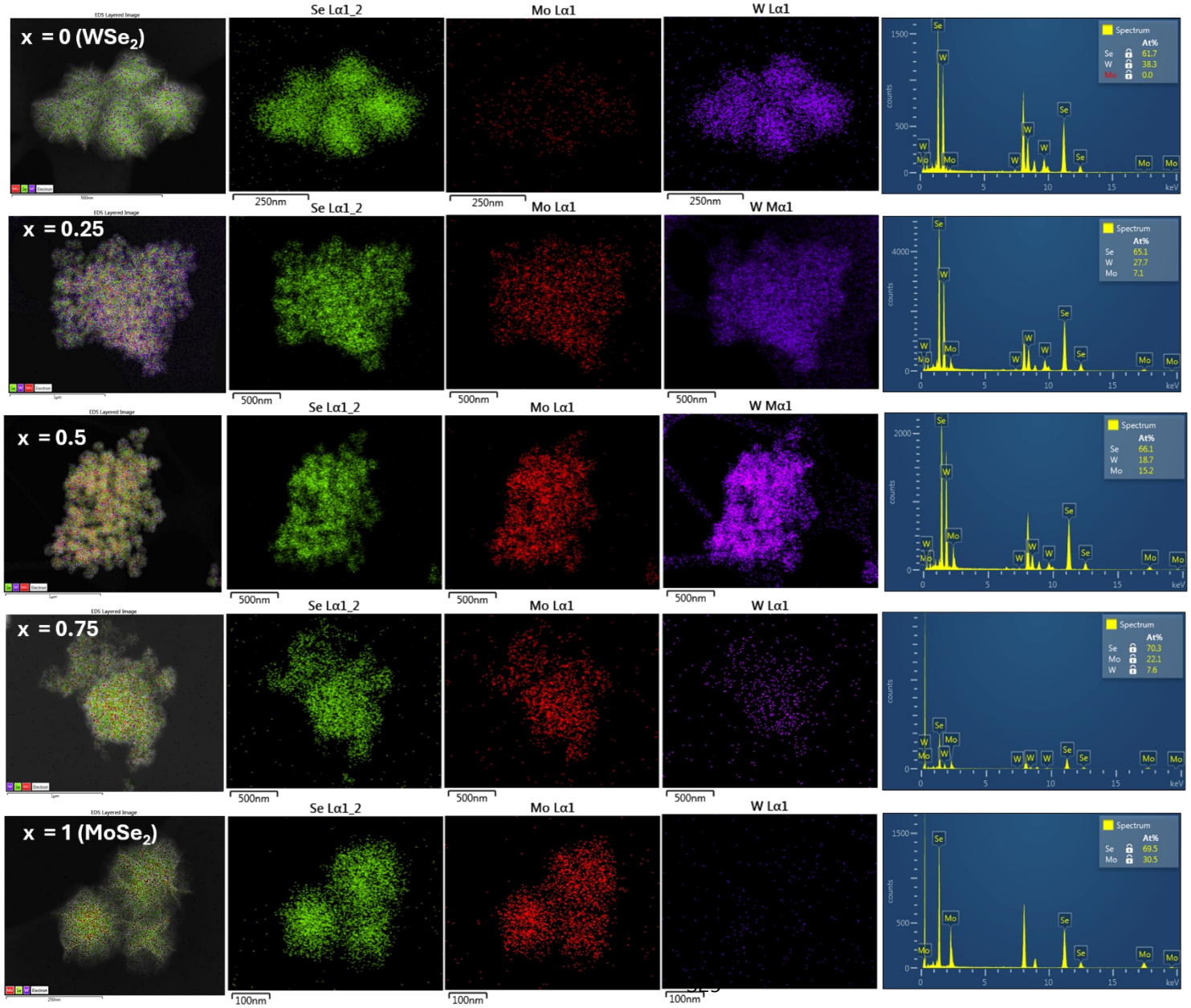
x = 0 (WSe2)
Se Lα1_2
Mo Lα1
W Lα1
250nm
Spectrum
At%
Se 61.7
W 38.3
Mo 0.0
x = 0.25
Se Lα1_2
Mo Lα1
W Mα1
500nm
Spectrum
At%
Se 65.1
W 27.7
Mo 7.1
x = 0.5
Se Lα1_2
Mo Lα1
W Mα1
500nm
Spectrum
At%
Se 66.1
W 18.7
Mo 15.2
x = 0.75
Se Lα1_2
Mo Lα1
W Lα1
500nm
Spectrum
At%
Se 70.3
Mo 22.1
W 7.6
x = 1 (MoSe2)
Se Lα1_2
Mo Lα1
W Lα1
100nm
Spectrum
At%
Se 69.5
Mo 30.5
counts
keV

$r_P = 4$

	$W_1Se_{2.42}$ (220 ℃)	$W_1Se_{2.33}$ (260 ℃)	$W_1Se_{2.24}$ (300 ℃)
x = 0 (WSe_2)	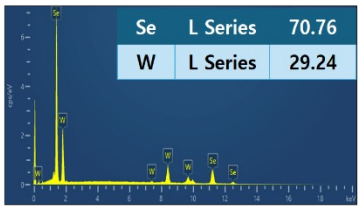	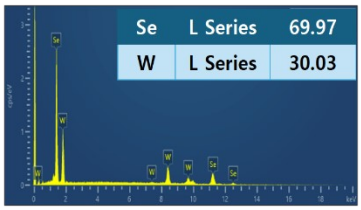	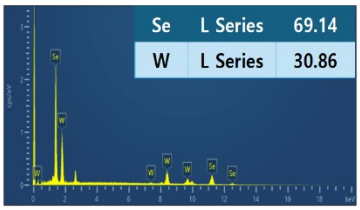
	$W_{77.01}Mo_{22.99}Se_{2.23}$ (220 ℃)	$W_{75.01}Mo_{24.99}Se_{2.19}$ (260 ℃)	$W_{70.83}Mo_{24.99}Se_{2.17}$ (300 ℃)
x = 0.25	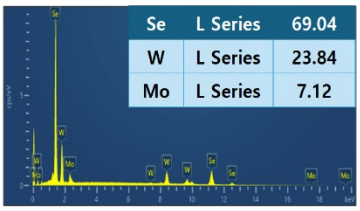	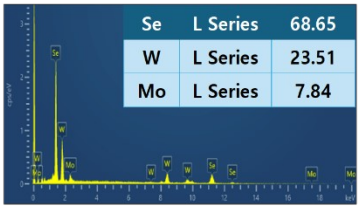	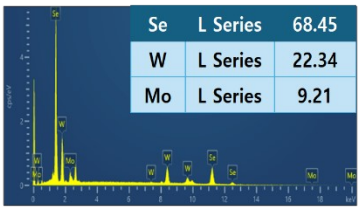
	$W_{52.92}Mo_{47.08}Se_{2.36}$ (220 ℃)	$W_{50.33}Mo_{49.67}Se_{2.09}$ (260 ℃)	$W_{51.83}Mo_{48.02}Se_{2.09}$ (300 ℃)
x = 0.5	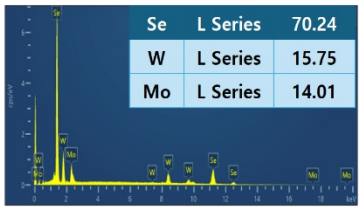	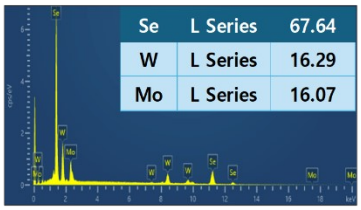	
	$W_{30.23}Mo_{69.77}Se_{2.19}$ (220 ℃)	$W_{26.72}Mo_{73.28}Se_{2.09}$ (260 ℃)	$W_{24.95}Mo_{75.05}Se_{2.16}$ (300 ℃)
x = 0.75	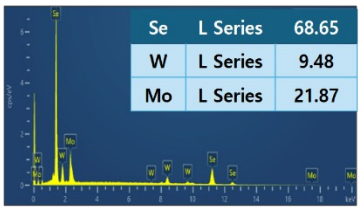	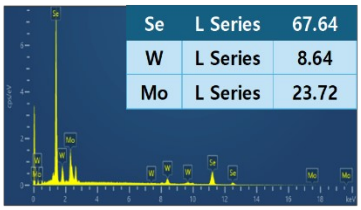	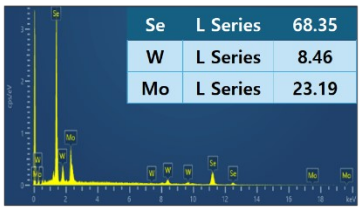
	$Mo_1Se_{2.17}$ (220 ℃)	$Mo_1Se_{2.09}$ (260 ℃)	$Mo_1Se_{2.06}$ (300 ℃)
x = 1 ($MoSe_2$)	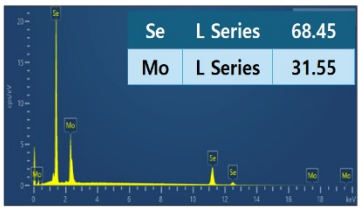	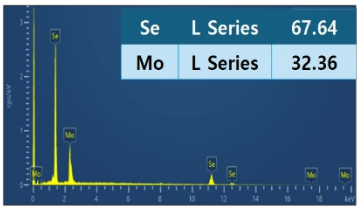	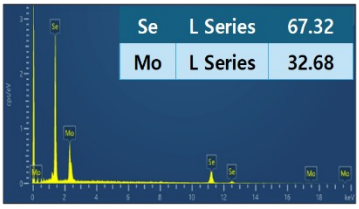

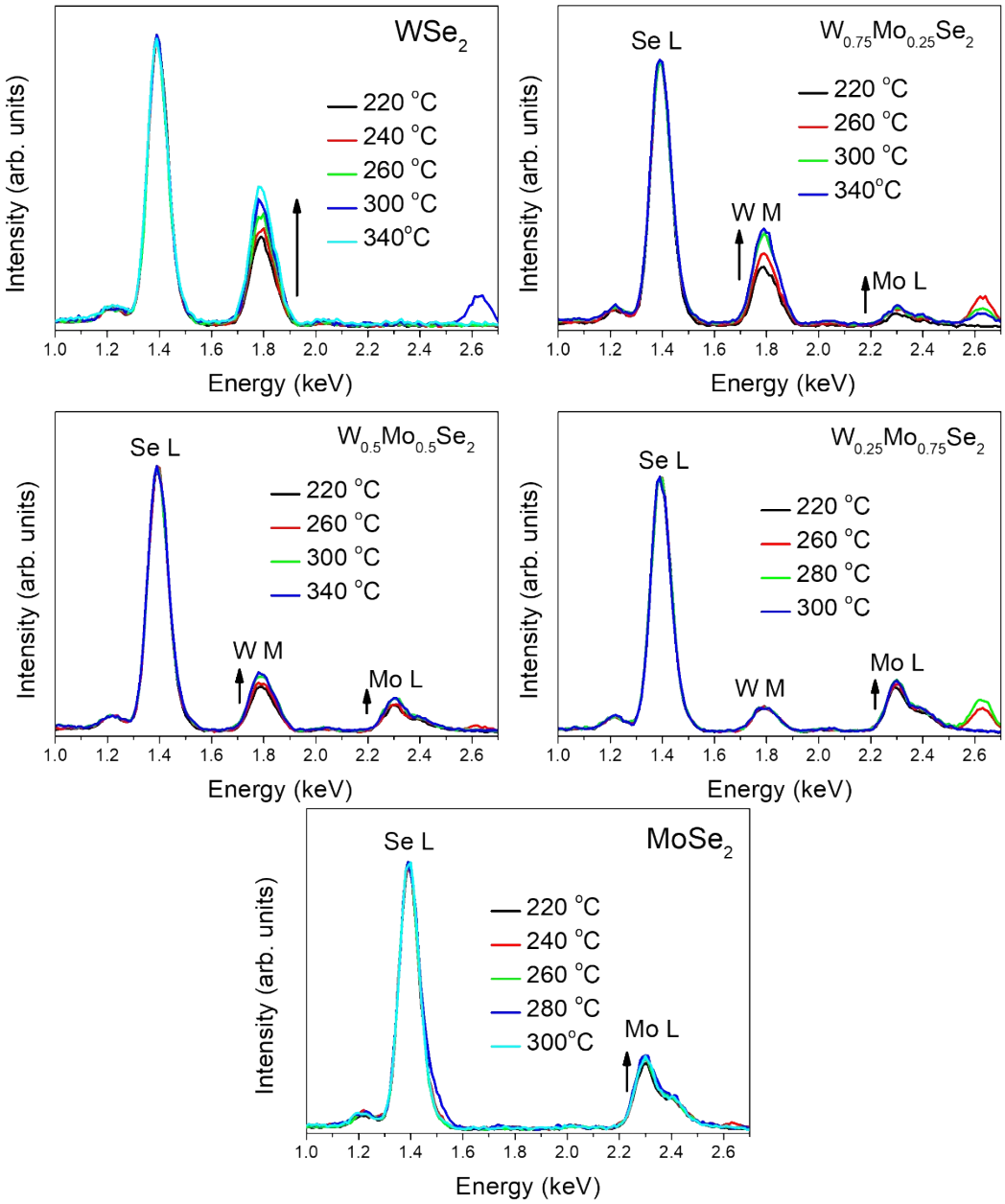
WSe2
220 °C
240 °C
260 °C
300 °C
340°C
Intensity (arb. units)
Energy (keV)
W0.75Mo0.25Se2
Se L
W M
Mo L
220 °C
260 °C
300 °C
340°C
W0.5Mo0.5Se2
220 °C
260 °C
300 °C
340 °C
W0.25Mo0.75Se2
220 °C
260 °C
280 °C
300 °C
MoSe2
220 °C
240 °C
260 °C
280 °C
300°C
1.0 1.2 1.4 1.6 1.8 2.0 2.2 2.4 2.6

(b)

	220 °C	260 °C	300 °C	340 °C
x = 0 (WSe_2)	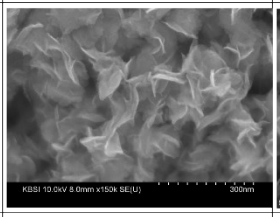	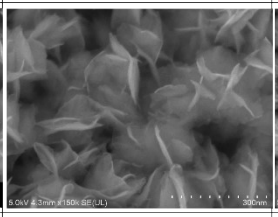	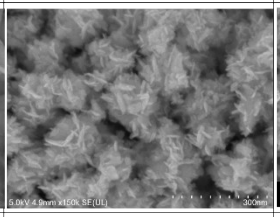	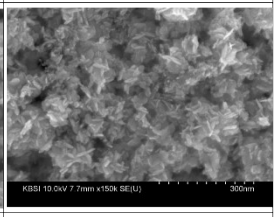
x = 0.25 ($W_{0.75}Mo_{0.25}Se_2$)	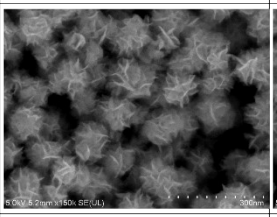	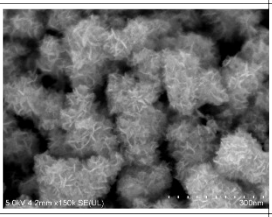	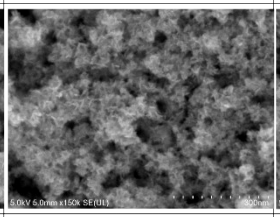	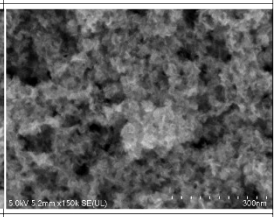
x = 0.5 ($W_{0.5}Mo_{0.5}Se_2$)	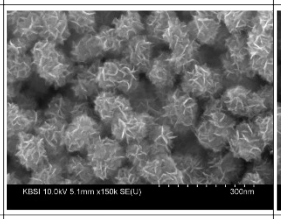	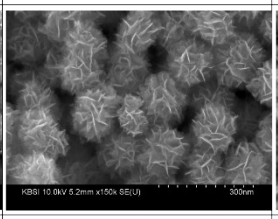	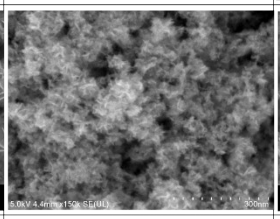	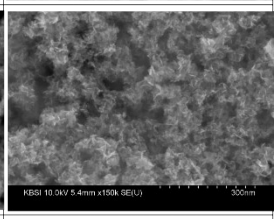
x = 0.75 ($W_{0.25}Mo_{0.75}Se_2$)	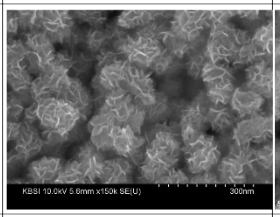	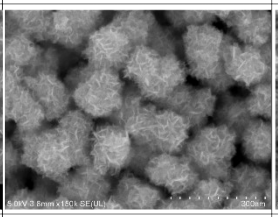	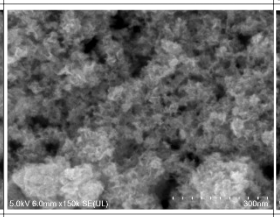	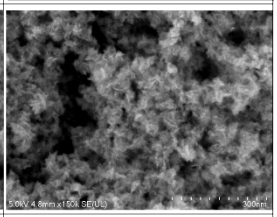
x = 1 ($MoSe_2$)	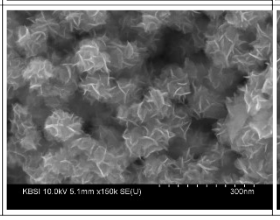	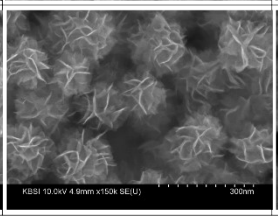	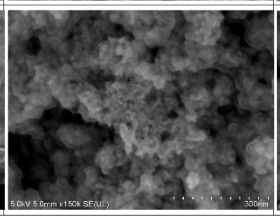	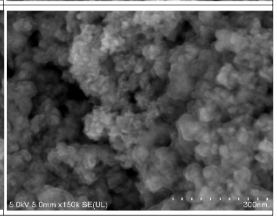

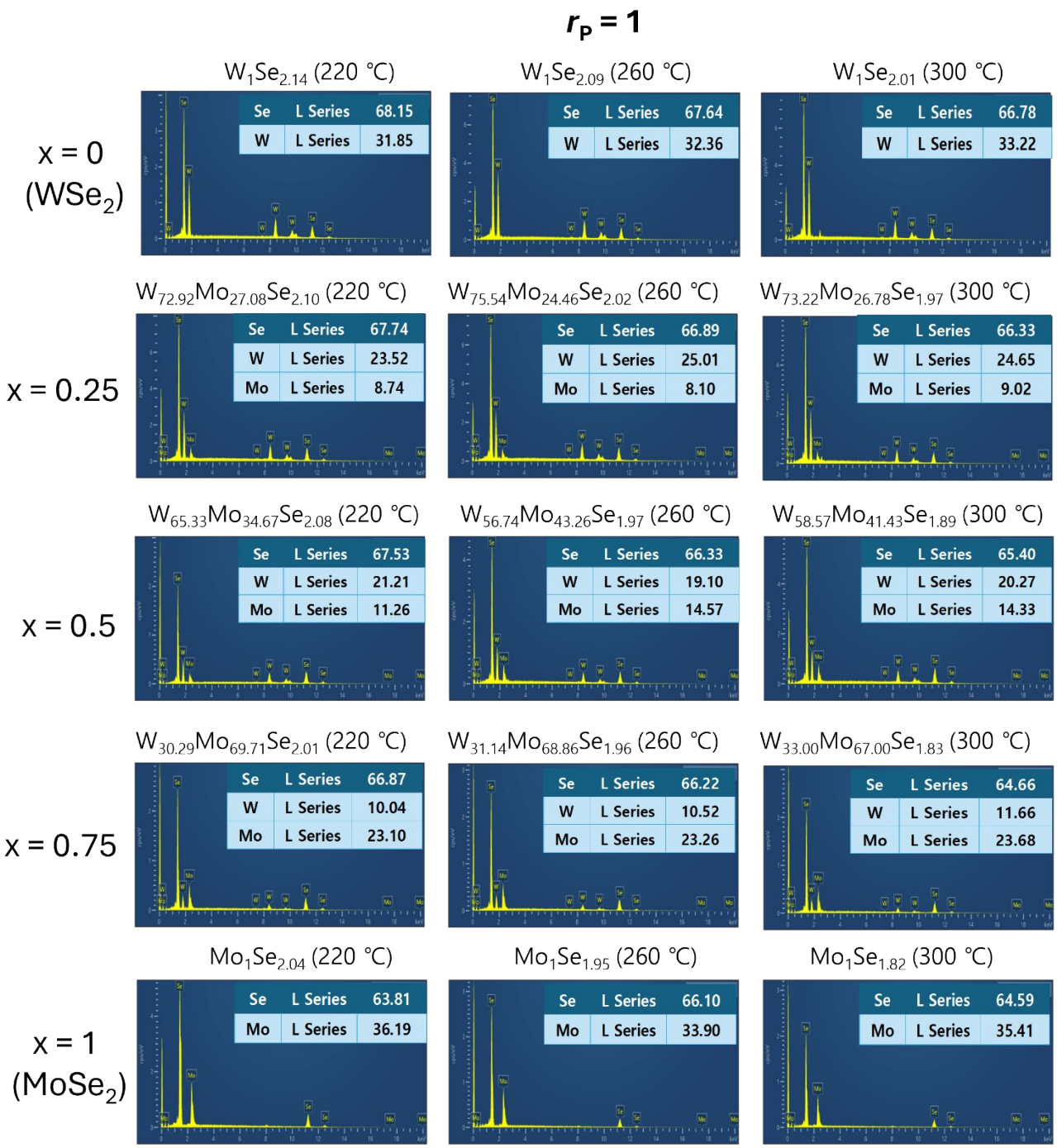

Figure S1. SEM, HRTEM, and EDX data of $W_{1-x}Mo_xSe_2$ (at x = 0, 0.25, 0.5, 0.75, and 1) nanosheet (NS) samples, synthesized using (a) r_P = [DBDS]/([WCl_6]+[$MoCl_5$]) = 4 and (b) r_P =1 at 220-340 °C.

The decrease of r_P from 4 to 1 didn't change the morphology and metal composition. Few-layer NSs assembled into flower-like nanoparticles. The WSe_2 (x = 0) NSs resembled petals (thickness: ~4 nm) of nanoflowers (size: ~150 nm). As x increased, the NSs became thinner, and the size of the nanoflowers decreased. $MoSe_2$ (x = 1) had a thickness of 2 ± 1 nm and the NSs were bundled into nanoparticles with a size of ~100 nm. When the growth temperature increased to 300 °C, the NSs aggregated to random sizes. EDX elemental mapping of W, Mo,

and Se with the HAADF-STEM images confirmed the homogeneous distribution of these elements in the entire NS flowers. The EDX spectrum of x = 0, 0.25, 0.5, 0.75, and 1 showed that the relative intensity of the Mo/W peaks *vs.* Se increased with increasing growth temperature, indicating that Se enrichment decreases at higher temperature (see Table S1). The x value (Mo content) measured for each sample matched well with that of the precursors.

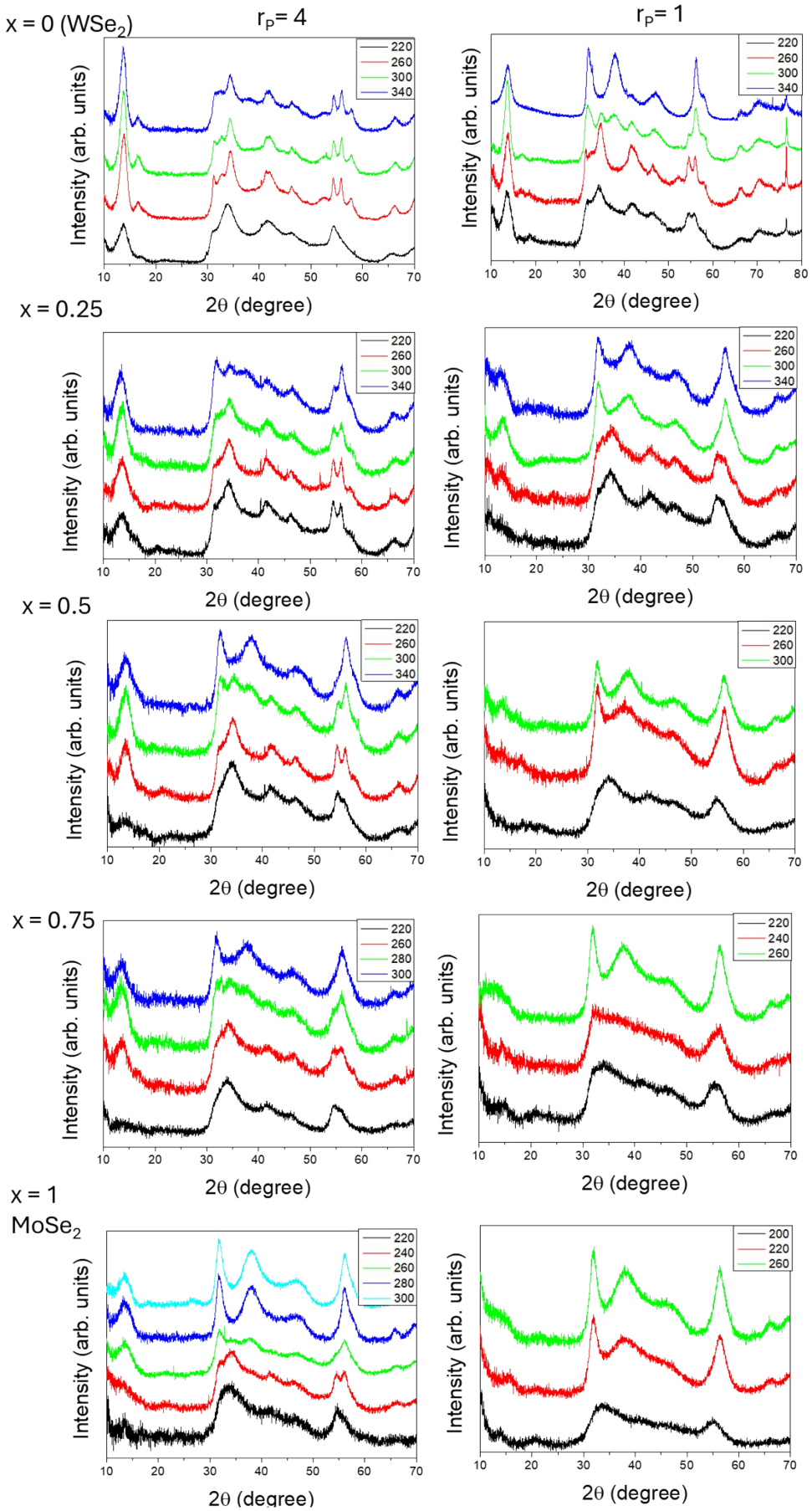
x = 0 (WSe2)
rP= 4
rP= 1
x = 0.25
x = 0.5
x = 0.75
x = 1
MoSe2
Intensity (arb. units)
2θ (degree)
220
240
260
280
300
340
200

Figure S2. XRD patterns of $W_{1-x}Mo_xSe_2$ samples synthesized using r_P = 4 and 1 at various temperatures.

The peaks of WSe_2 (r_P = 4 at 200-340 °C) matched the reference peaks of 2M (a = 5.87 Å, b = 3.31 Å, c = 13.8 Å, and β = 110°). At 340 °C, the $(103)_{2H}$ peak at 2θ = 38° appeared with a weak intensity, indicating that the phase conversion starts to occur. If the reaction temperature is higher, the 2H phase peaks would be intense, which makes clear to define the T_{2M}. However, the use of OA as solvent limit the temperature due to the boiling point (360 °C). With r_P = 1, the 2H phase peaks start to appear at 300 °C, and becomes dominant at 340 °C. The peaks matched the reference peaks of 2H phase WSe_2 (a = 3.273 Å and c = 13.04 Å), which are nearly identical to the reference values (JCPDS No. 87-2418; $P6_3/mmc$, a = 3.286 Å and c = 12.980 Å). The results indicate that r_P = 1 reduced T_{2M} to 300 °C. In the case of $MoSe_2$ (r_P = 4), the 2H peak at 2θ = 38° appear at 240 °C, and becomes dominant at higher temperatures. At r_P = 1, the 2H peak appears at 220 °C (r_P = 4), suggesting T_{2M} = ~200 °C. The 2M phase peaks matched the reference peaks of 2M phase $MoSe_2$ (a = 5.98 Å, b = 3.29 Å, c = 14.3 Å, and β = 113°). The 2H phase peak matched the reference peaks of 2H phase $MoSe_2$ (JCPDS No. 29-0914; $P6_3/mmc$, a = 3.287 Å and c = 12.925 Å). Therefore, T_{2M} = 240 and 200 °C was determined for r_P = 4 and 1, respectively. In this way, T_{2M} of the alloys was determined, as shown in Figure 1e.

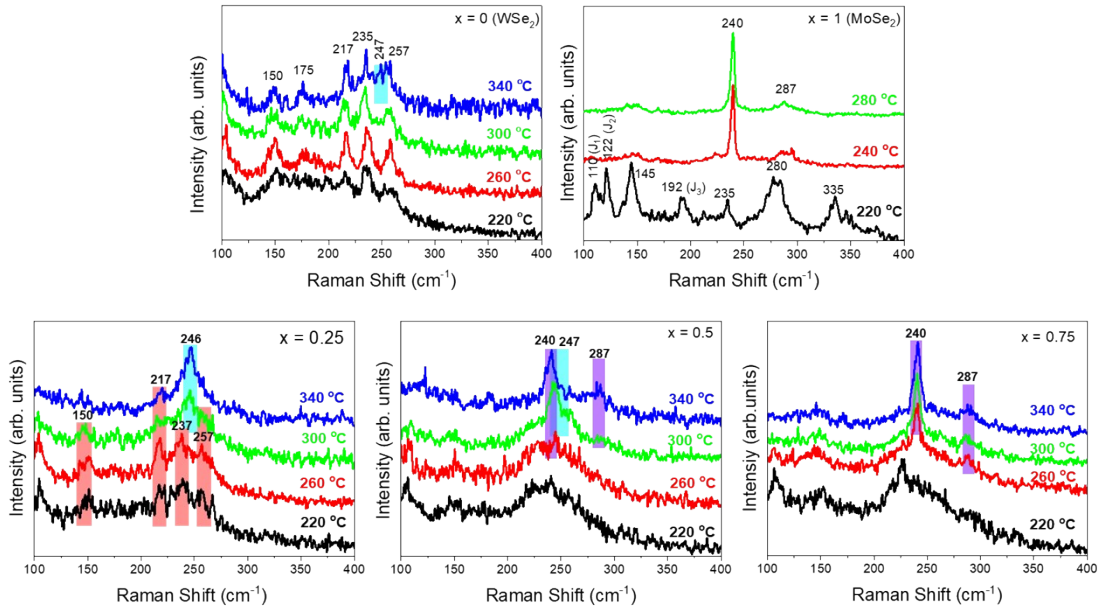

Figure S3. Raman spectra of $W_{1-x}Mo_xSe_2$ NSs (at x = 0, 0.25, 0.5, 0.75, and 1) synthesized using r_P = 4 at 220-340 °C. The excitation source was a 532 nm diode laser.

WSe_2 shows typical 2M phase peaks at all temperatures: 150 cm^{-1}, 175 cm^{-1}, 235, and 257 cm^{-1}.[S41] At 340 °C, the peak at 247 cm^{-1} appears, which is assigned to the unresolved in-plane E^1_{2g} and out-of-plane A_{1g} vibration modes. $MoSe_2$ at 220 °C shows the unique peaks of 2M (or 1T') phase: the J_1 peak at 110 cm^{-1}, the J_2 peak at 122 cm^{-1}, and the J_3 peak at 192 cm^{-1}.[S42] The peak at 145 cm^{-1} was assigned to the E_{1g} mode. The 240/280 °C samples show the 2H phase peaks at 240 and 287 cm^{-1}, corresponding to the out-of-plane A_{1g} and in-plane E^1_{2g} vibration modes, respectively. The x = 0.25 at 220-300 °C shows the 2M phase WSe_2 peaks, but the 2H phase peak at 246 cm^{-1} becomes dominant at 340 °C. The x = 0.5 at 220 and 260 °C show the broad 2M peaks. At 300 and 340 °C, the 2H WSe_2 peak at 247 cm^{-1} exists with the 2H $MoSe_2$ peaks at 240 cm^{-1} and 287 cm^{-1}. The x = 0.75 at 220 °C show the broad 2M peaks. At 260-340 °C, the 2H $MoSe_2$ peaks at 240 cm^{-1} and 287 cm^{-1} became more dominant with increasing temperature. Therefore, the Raman spectrum confirmed that the T_{2M} decreases with increasing x.

Survey

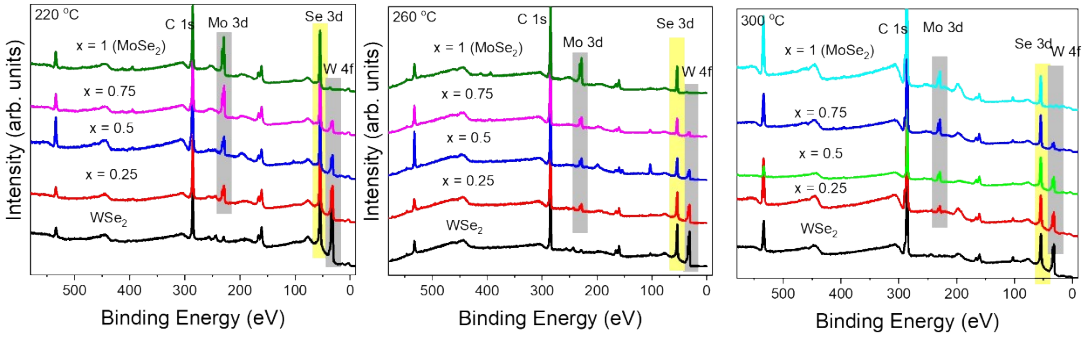

Valence Band

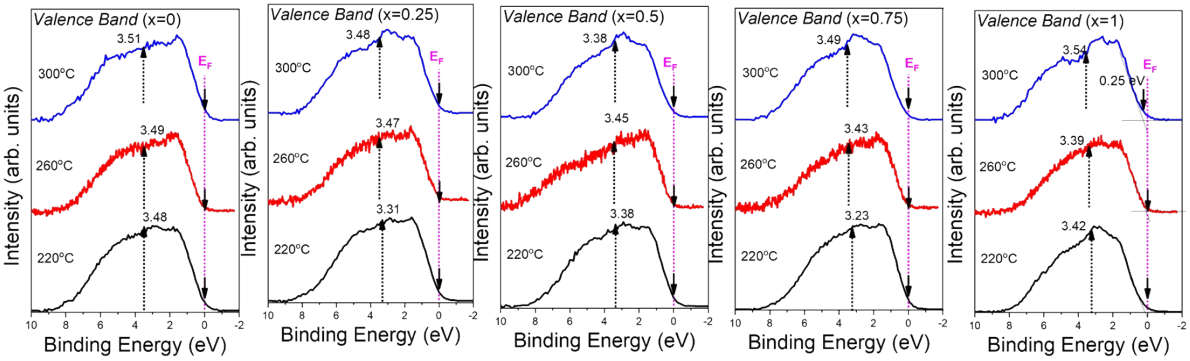

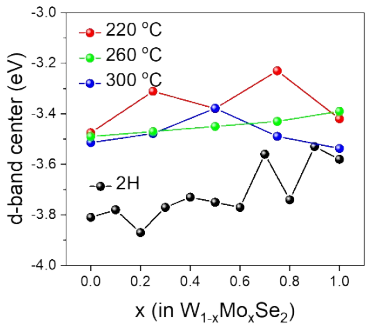

x = 0 (WSe_2)

x = 1 ($MoSe_2$)

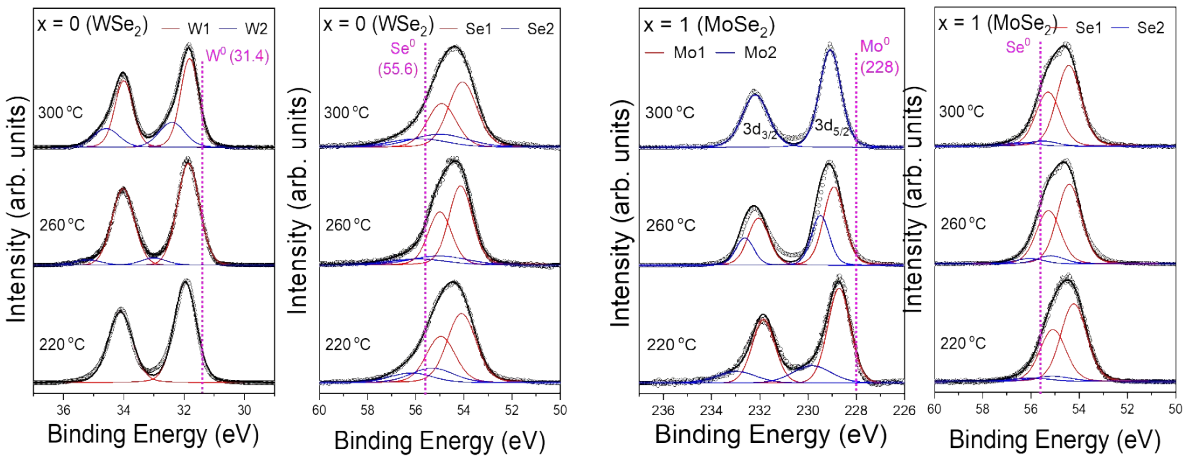

x = 0.25 ($W_{0.75}Mo_{0.25}Se_2$)

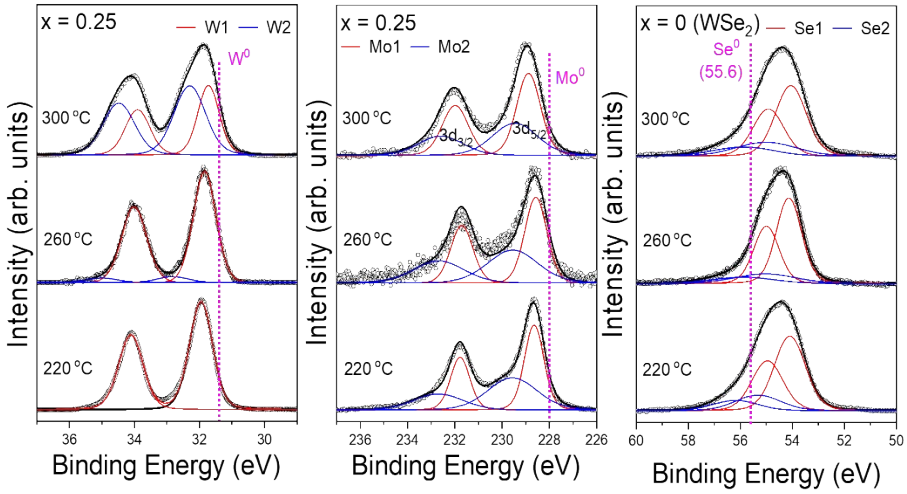

x = 0.5 ($W_{0.5}Mo_{0.5}Se_2$)

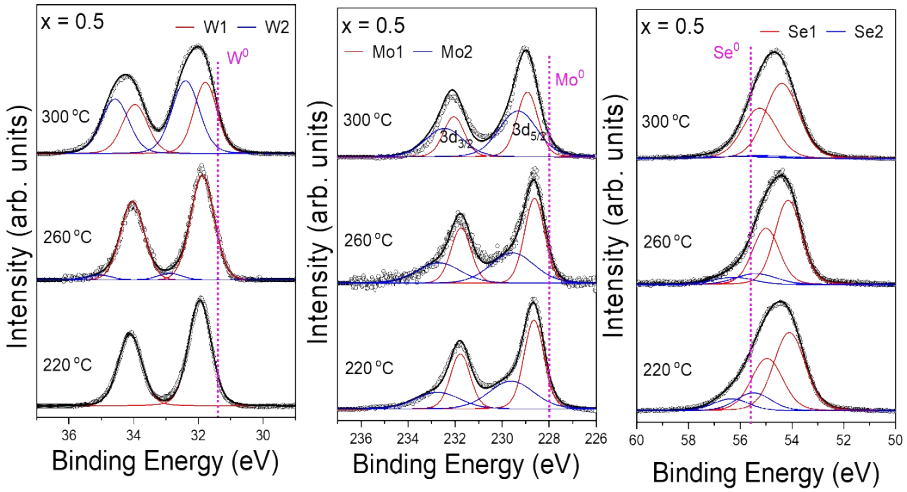

x = 0.75 ($W_{0.25}Mo_{0.75}Se_2$)

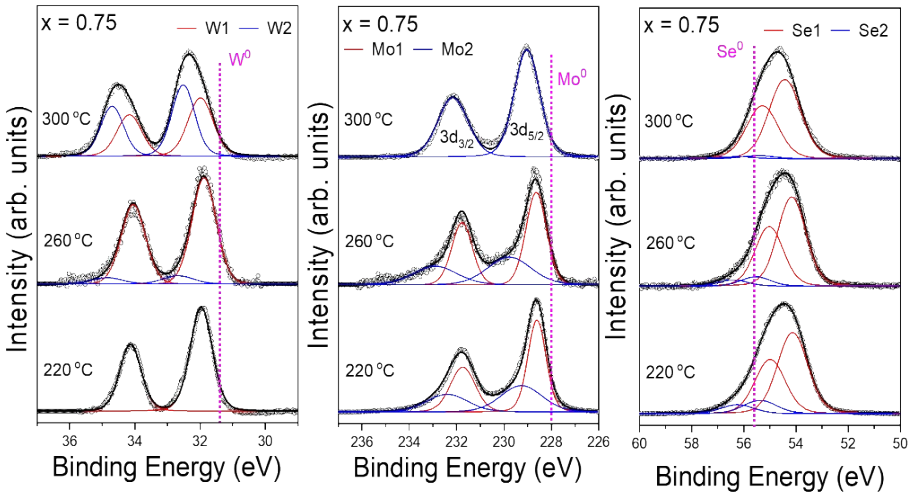

Figure S4. XPS survey scan, valence band spectrum (VBS), and *d*-band center *vs. x*. Fine-scanned W 4*f*, Mo 3*d*, and Se 3d of $W_{1-x}Mo_xSe_2$ (at $x = 0$, 0.25, 0.5, 0.75, and 1) NSs synthesized using $r_P = 4$ at 220, 260, and 300 °C. Photon energy is 650 eV. Normalized XPS VBS, plotted to show the *d*-band center position (the weight center of the VBS derived by integration), which is marked by the arrow. The raw data (open circles) of fine-scanned peaks are fitted by a Voigt function, and the sum of the resolved bands is represented by the black line. The position of neutral W^0 ($4f_{7/2}$ at 31.4 eV), Mo^0 ($3d_{5/2}$ at 228.0 eV), Se^0 ($3d_{5/2}$ at 55.6 eV), and Fermi level (E_F) is marked by dotted vertical line.

Survey scan shows that the relative peak intensity of Mo *vs.* W increases with increasing *x*, supporting the successful composition tuning.

The XPS valence band spectra (VBS) were obtained by the background correction with a Shirley-type baseline. The positions of the valence band maximum (E_{VBM}) below the Fermi level (E_F) were evaluated by linear extrapolation of the onset in the XPS VBS. It confirmed that most samples exhibit the metallic properties with $E_{VBM} = 0$ eV, except $MoSe_2$ ($E_{VBM} = 0.25$ eV) at 300 °C. We reported E_{VBM} = 0.54 and 0.52 eV for 2H phase WSe_2 and $MoSe_2$, respectively.[S24] Therefore, $MoSe_2$ at 300 °C is more metallic than the 2H $MoSe_2$.

By the integration of VBS up to 10.0 eV with respect to E_F, we obtained the weight center as the *d*-band center (ε_d). The position is marked by arrows. The higher 2H character increase the ε_d value. The samples at 220 °C exhibit the smaller negative values (ε_d = -3.5 ~ -3.2 eV) than 2H phase WSe_2 phase (ε_d = -3.9 ~ -3.6 eV), due to the more metallic characters.[S24] As the growth temperature increases to 300 °C, ε_d of x = 0.75 and 1 shifts to more negative values because of the phase conversion into the 2H phase.

The W $4f_{7/2}$ and $4f_{5/2}$ peaks are separated by 2.18 eV. The peak was resolved into two bands; W1 band at 31.9 eV and W2 band at 32.3-32.5 eV for $4f_{7/2}$ peak, which are assigned to the 2M and 2H phases, respectively. As the temperature or *x* increases, the fraction of 2H phase increases.

The Mo $3d_{5/2}$ and $3d_{3/2}$ peaks are separated by 3.13 eV. The Mo1 band at 229 eV and Mo2 band at 230 eV for $3d_{5/2}$ peak are assigned to 2M and 2H phase, respectively. As the temperature or *x* increases, the fraction of the 2H phase increases, and it becomes 100% at x = 0.75 and 1 at 300 °C.

The Se peak appears at 54.0-54.2 eV. The Se $3d_{5/2}$ and $3d_{3/2}$ peaks are separated by 0.86 eV. The peak was resolved into two bands (S1 and Se2). The S1 band ($3d_{5/2}$) redshifts from neutral Se peak (Se^0) at 55.6 eV by approximately 1.5 eV and is assigned to the Se-metal bonding structure. The Se2 band at 55-56 eV for $3d_{5/2}$ peak is assigned to the Se-Se bonding of the excess Se atoms. The fraction of the Se2 band decreases as the temperature or *x* increases.

We summarized the XPS data as follows. As the temperature increases, the fraction of 2H phase increases, which is more significant at higher *x*.

WSe_2 (x = 0)

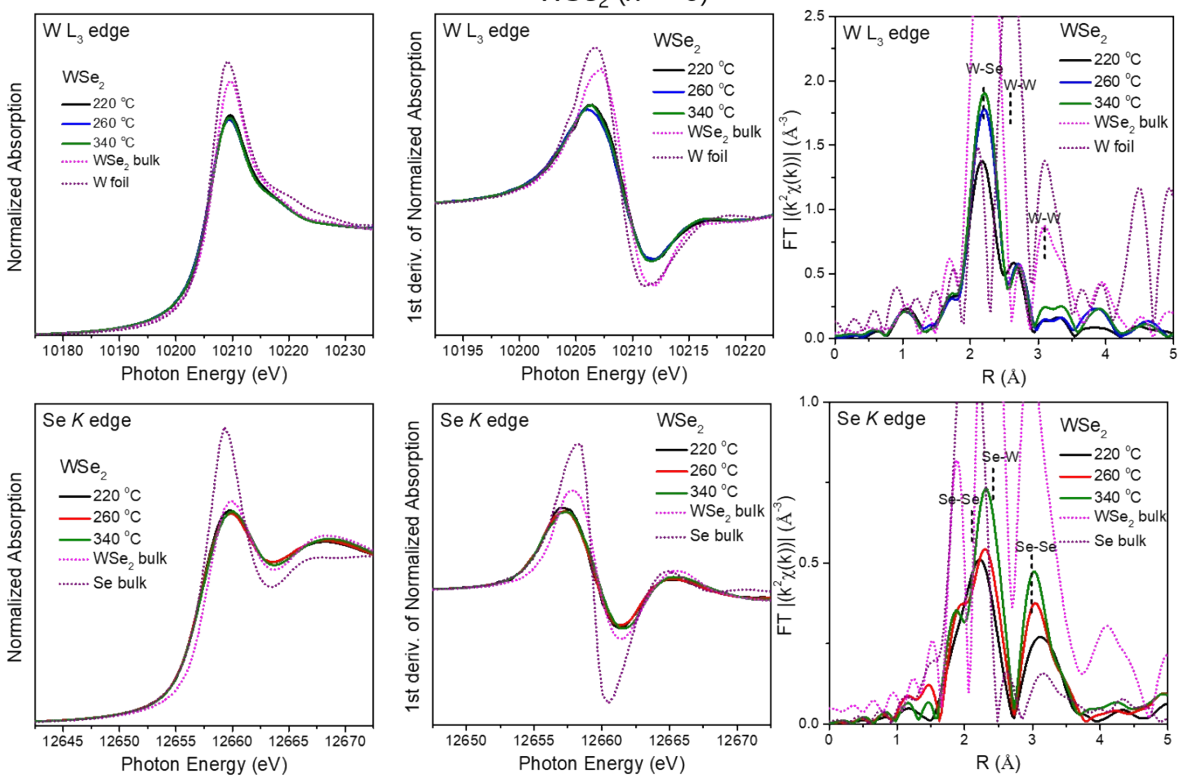

$MoSe_2$ (x = 1)

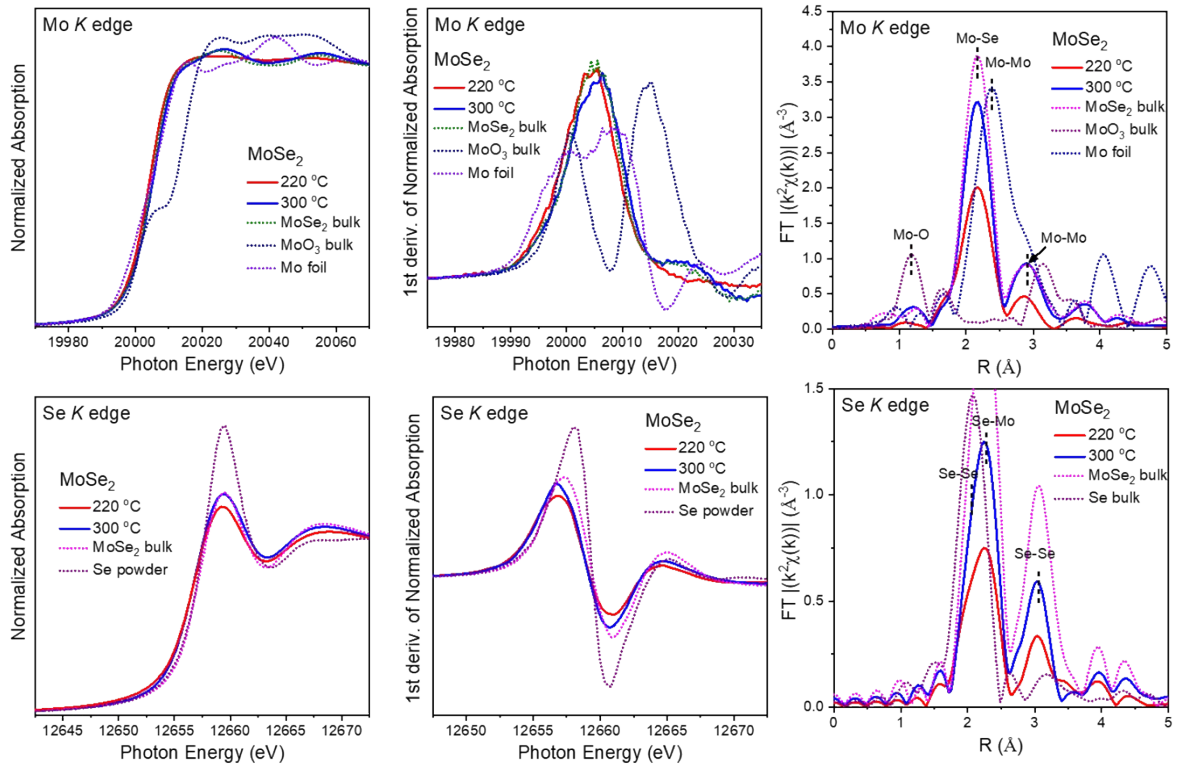

x_{Mo} = 0.25

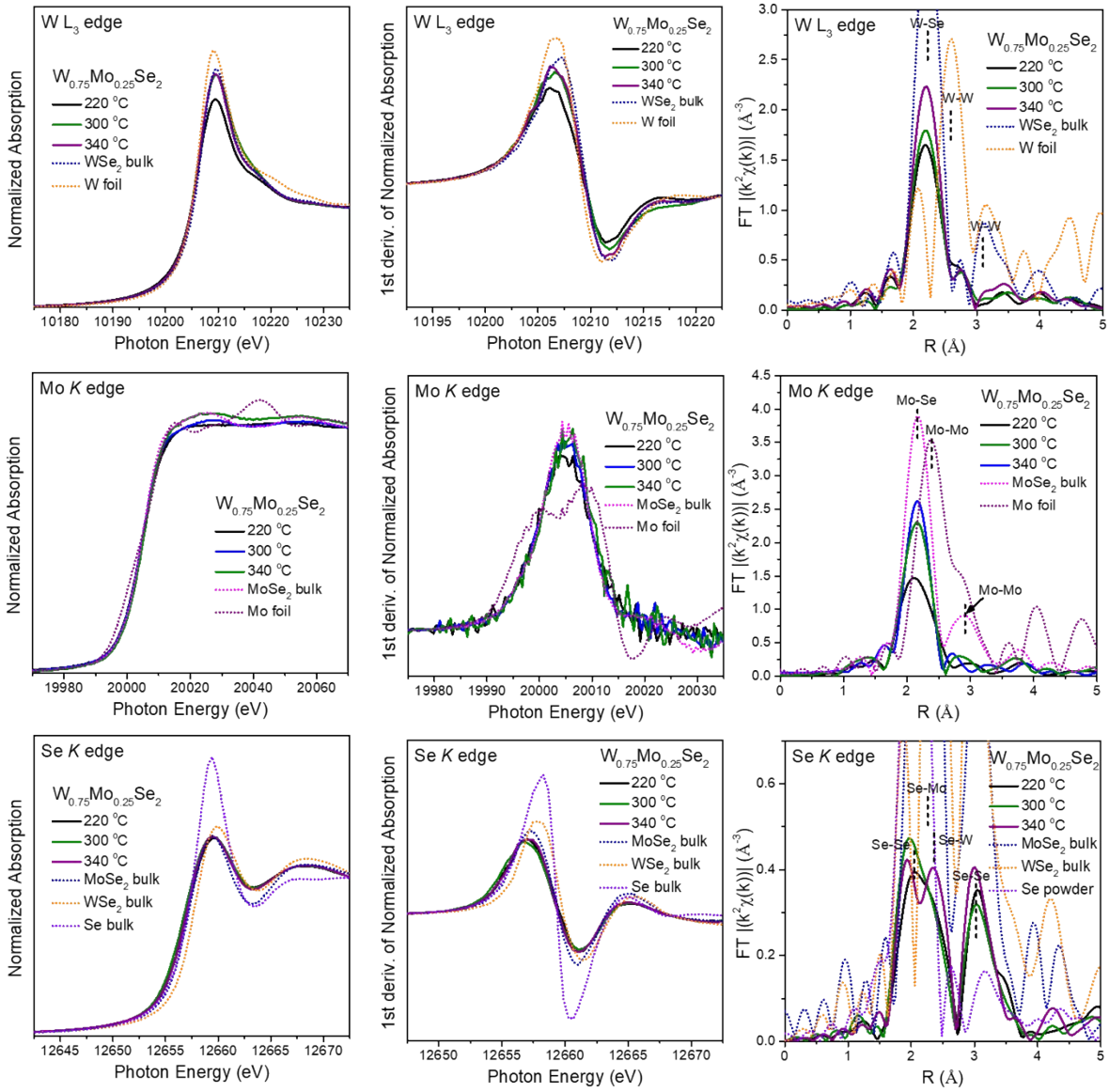
W L3 edge
W0.75Mo0.25Se2
220 °C
300 °C
340 °C
WSe2 bulk
W foil
Normalized Absorption
Photon Energy (eV)
1st deriv. of Normalized Absorption
W-Se
W-W
FT |(k2χ(k)| (Å-3)
R (Å)
Mo K edge
MoSe2 bulk
Mo foil
Mo-Se
Mo-Mo
Se K edge
Se bulk
Se powder
Se-Se
Se-Mo
Se-W

x_{Mo} = 0.5

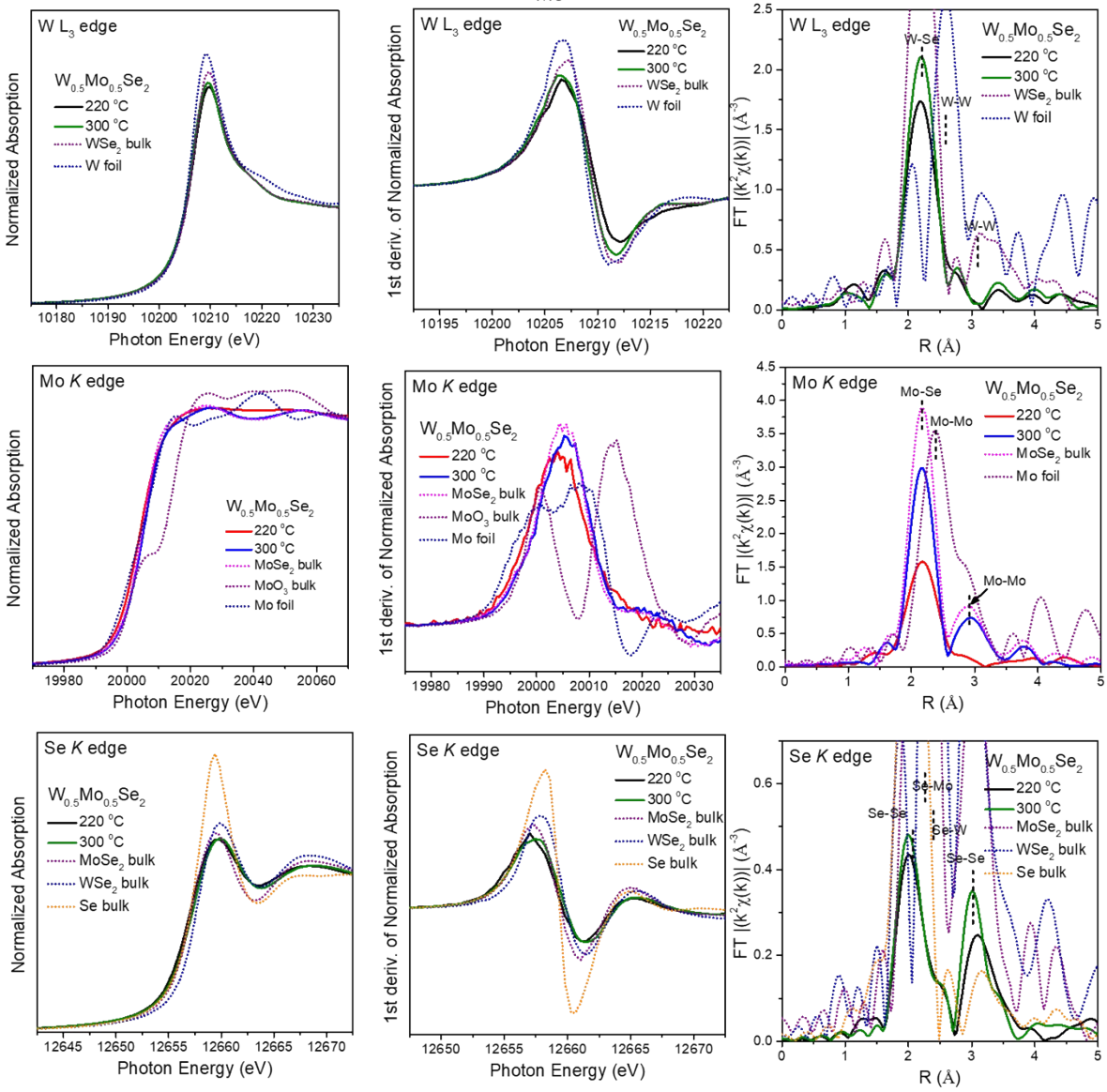
W L3 edge
W0.5Mo0.5Se2
220 °C
300 °C
WSe2 bulk
W foil
Normalized Absorption
Photon Energy (eV)
1st deriv. of Normalized Absorption
FT |(k2χ(k))| (Å-3)
R (Å)
W-Se
W-W
Mo K edge
MoSe2 bulk
MoO3 bulk
Mo foil
Mo-Se
Mo-Mo
Se K edge
Se bulk
Se-Se
Se-Mo
Se-W

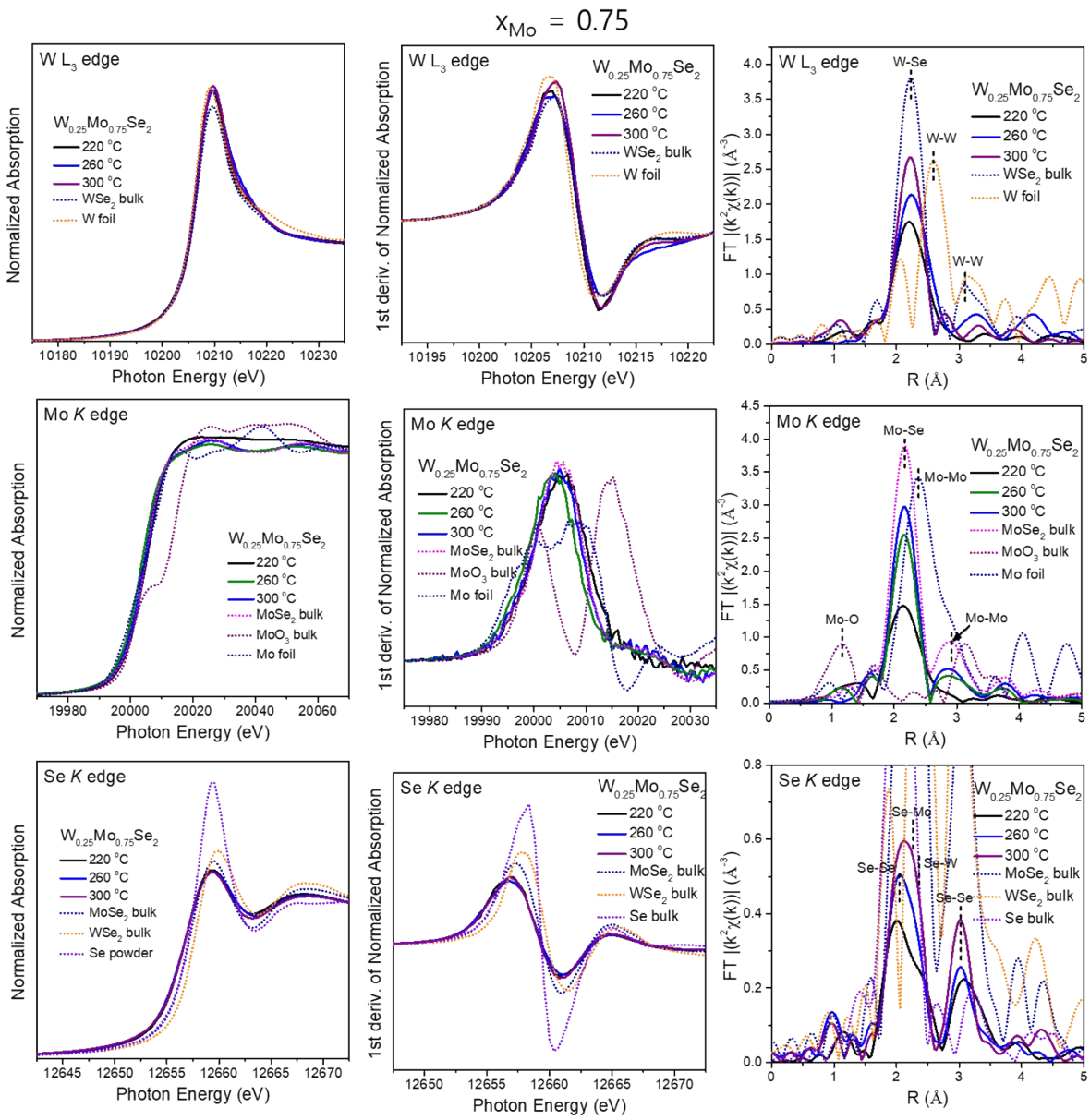

Figure S5. XANES, 1st derivate of XANES, and k^2-weighted FT-EXAFS above W L_3 edge, Mo K edge, and Se K edge of $W_{1-x}Mo_xSe_2$ NSs synthesized using r_P = 4 at 220-340 °C. Interatomic distance and coordination number (CN) were obtained by the curve fitting. The fitting parameters are summarized in **Table S2**. As the temperature or *x* increases, the white line intensity of XANES of W and Mo atoms increases owing to the greater semiconducting character. As the temperature increases, the peak intensity of EXAFS increases because of fewer metal vacancies, and the fraction of the 2H phase increases more significantly at higher *x* values.

	2H WSe_2	2M WSe_2	1T' WSe_2	2H $MoSe_2$	2M $MoSe_2$	1T' $MoSe_2$
[001]	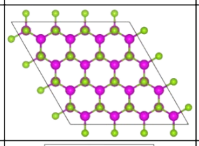	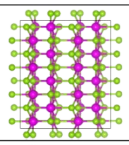	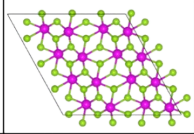	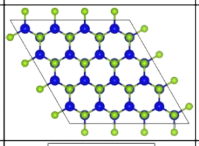	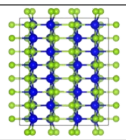	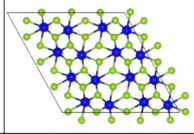
[010]	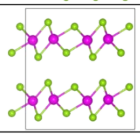	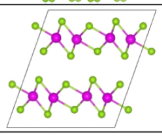	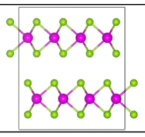	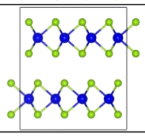	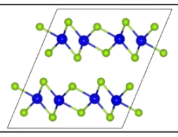	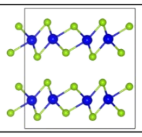
E_{rel}	0	103.031 meV	111.240 meV	0	116.944 meV	123.615 meV
E_{rel}^{U}	0	85.004 meV	91.985 meV	0	83.256 meV	92.151 meV

	2H $W_{0.75}Mo_{0.25}Se_2$					
[001]	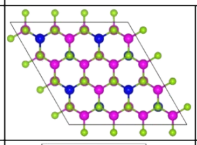	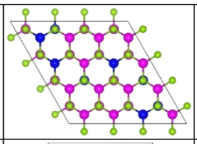	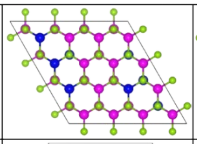	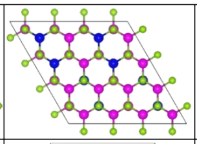	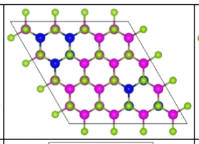	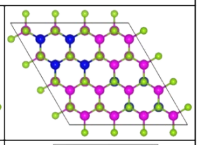
[010]	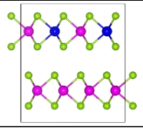	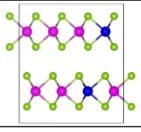	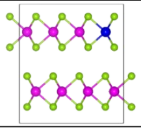	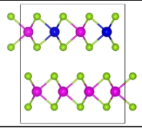	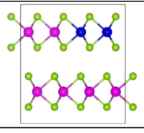	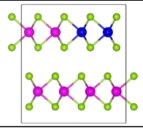
E_{rel}	0	0.363 meV	0.630 meV	0.658 meV	0.974 meV	1.526 meV
E_{rel}^{U}	0	0.393 meV	0.703 meV	0.725 meV	1.070 meV	1.699 meV

	2M $W_{0.75}Mo_{0.25}Se_2$					
[001]	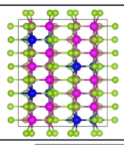	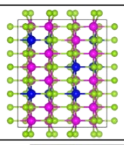	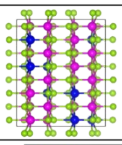	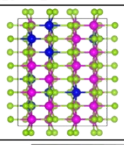	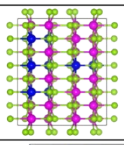	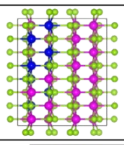
[010]	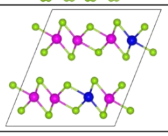	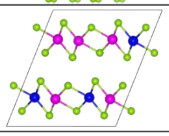	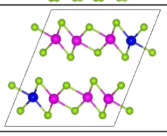	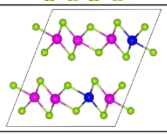	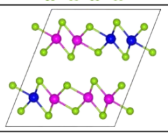	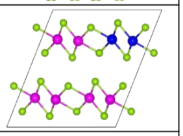
E_{rel}	0	0.179 meV	0.370 meV	0.430 meV	0.613 meV	3.451 meV
E_{rel}^{U}	0	0.221 meV	0.538 meV	1.166 meV	0.495 meV	1.880 meV

	1T' $W_{0.75}Mo_{0.25}Se_2$					
[001]	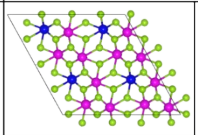	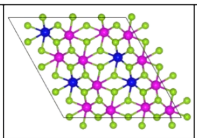	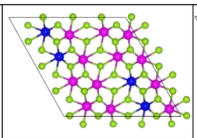	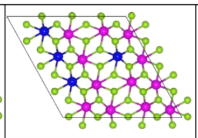	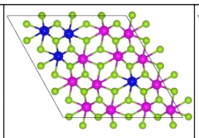	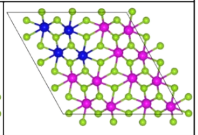
[010]	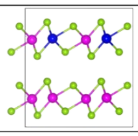	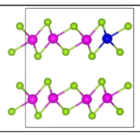	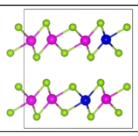	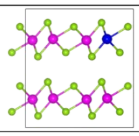	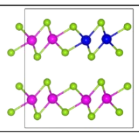	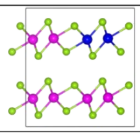
E_{rel}	0	0.198 meV	0.378 meV	0.433 meV	0.619 meV	1.064 meV
E_{rel}^{U}	0	0.297 meV	0.541 meV	0.595 meV	1.272 meV	1.997 meV

	2H $W_{0.5}Mo_{0.5}Se_2$					
[001]	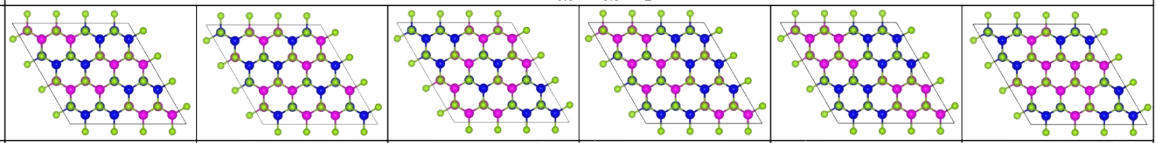					
[010]	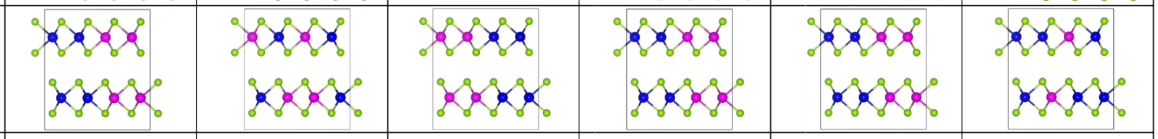					
E_{rel}	0	0.194 meV	0.228 meV	1.095 meV	1.122 meV	1.394 meV
E_{rel}^{U}	0	0.233 meV	0.262 meV	1.234 meV	1.254 meV	1.526 meV

	2M $W_{0.5}Mo_{0.5}Se_2$					
[001]	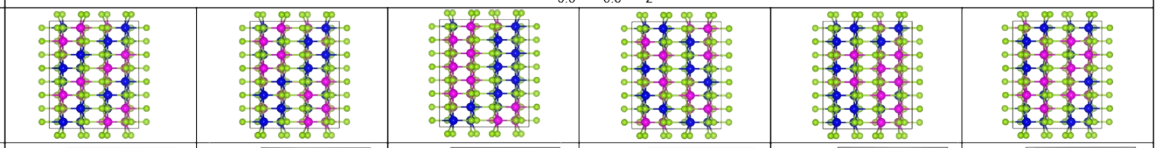					
[010]	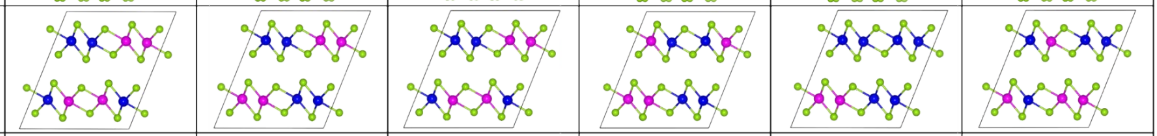					
E_{rel}	0	0.157 meV	0.385 meV	0.835 meV	0.860 meV	1.395 meV
E_{rel}^{U}	0	1.006 meV	1.044 meV	0.707 meV	1.363 meV	1.828 meV

	1T' $W_{0.5}Mo_{0.5}Se_2$					
[001]	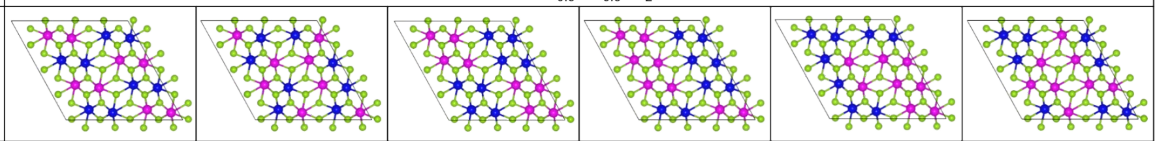					
[010]	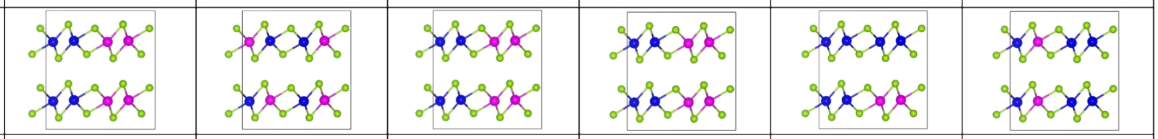					
E_{rel}	0	0.130 meV	0.186 meV	0.302 meV	0.779 meV	1.566 meV
E_{rel}^{U}	0.043 meV	0	0.798 meV	0.856 meV	1.147 meV	1.627 meV

	2H $W_{0.25}Mo_{0.75}Se_2$					
[001]	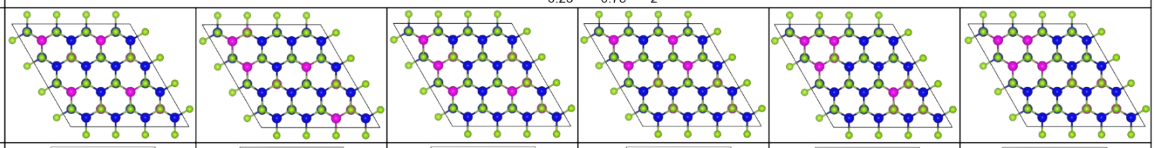					
[010]	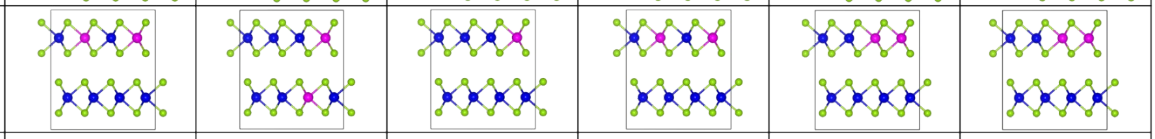					
E_{rel}	0	0.355 meV	0.630 meV	0.655 meV	0.965 meV	1.551 meV
E_{rel}^{U}	0	0.375 meV	0.687 meV	0.708 meV	1.052 meV	1.708 meV

	2M $W_{0.25}Mo_{0.75}Se_2$					
[001]	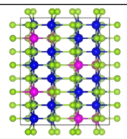	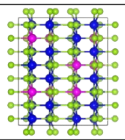	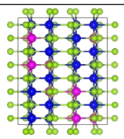	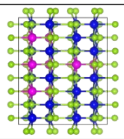	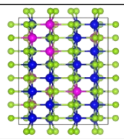	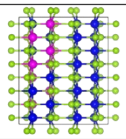
[010]	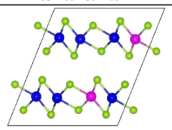	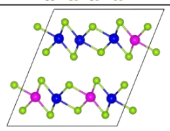	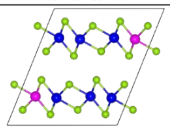	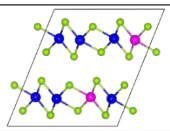	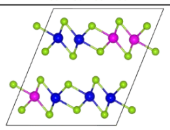	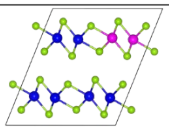
E_{rel}	0	0.186 meV	0.365 meV	0.453 meV	0.631 meV	1.140 meV
E_{rel}^{U}	0	0.335 meV	0.537 meV	0.630 meV	1.480 meV	2.234 meV

	1T' $W_{0.25}Mo_{0.75}Se_2$					
[001]	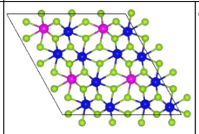	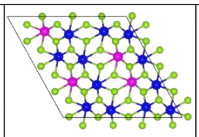	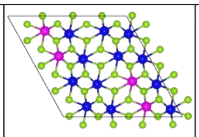	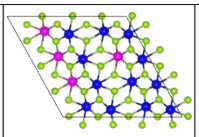	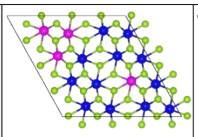	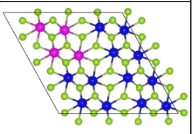
[010]	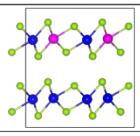	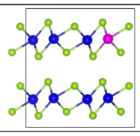	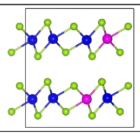	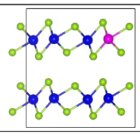	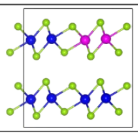	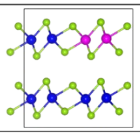
E_{rel}	0	0.208 meV	0.392 meV	0.467 meV	0.649 meV	1.152 meV
E_{rel}^{U}	0	0.313 meV	0.554 meV	0.628 meV	1.313 meV	0.815 meV

Figure S6. Configurations of pristine 2H, 2M, and 1T′ phase $W_{1-x}Mo_xSe_2$ at x = 0, 0.25, 0.5, 0.75, and 1, which were built from (4× 4 × 1) supercell with two layers. The relative energy (E_{rel} or E_{rel}^{U}) per atom is with respect to the most stable 2H phase, where E_{rel} and E_{rel}^{U} was calculated using DFT and DFT+U (U_{eff} = 2.6 eV for W and U_{eff} = 3.3 eV for Mo), respectively. Pink, blue, and green balls represent W, Mo, and Se atoms, respectively.

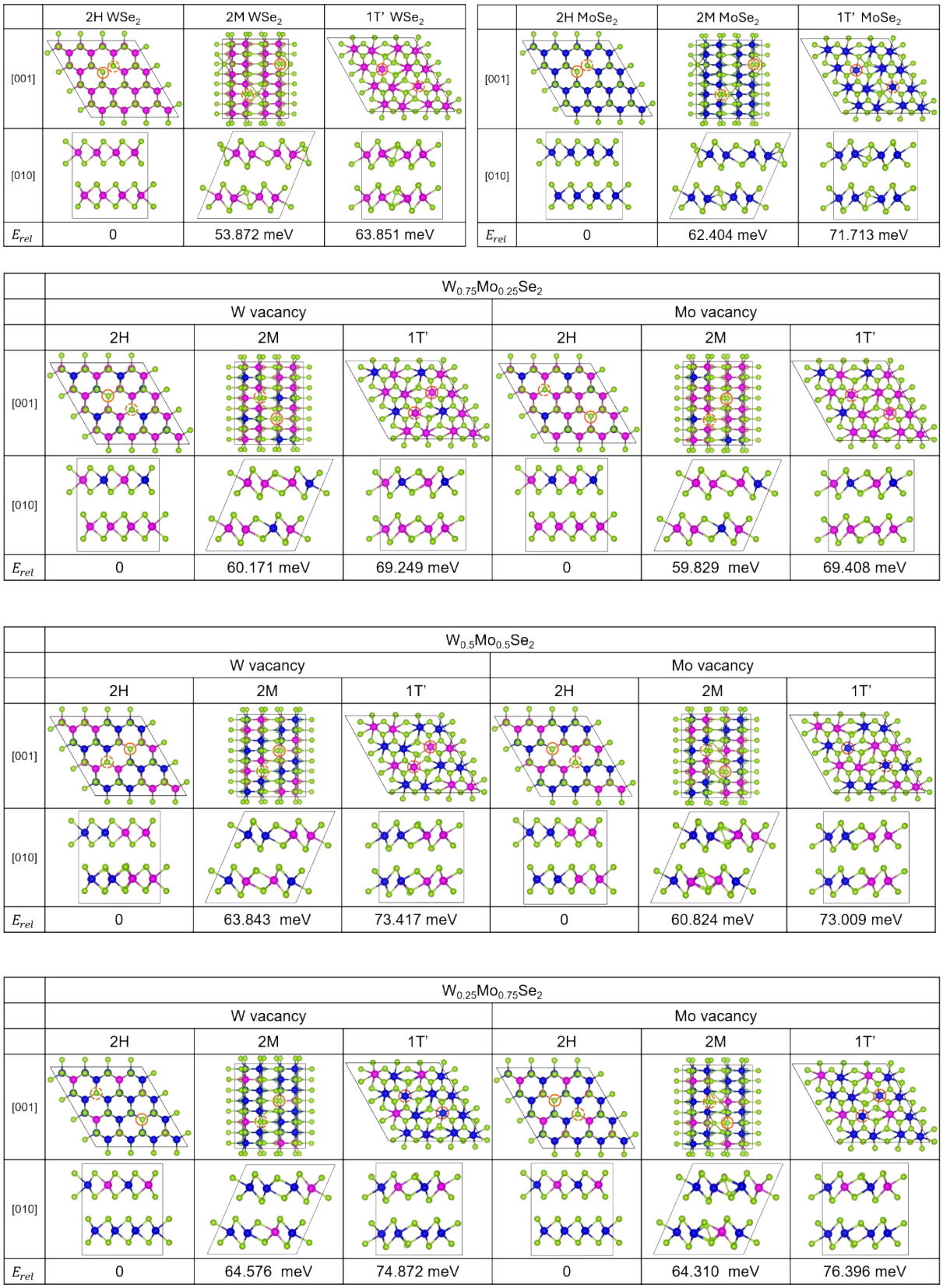

Figure S7. Configurations for metal vacancy (MV) model of 2H, 2M, and 1T′ phase $W_{1-x}Mo_xSe_2$ at x = 0, 0.25, 0.5, 0.75, and 1, which were built from (4× 4 × 1) supercell with two layers. They were projected along [001] and [010]. The relative energy (E_{rel}) per atom is with

respect to the most stable 2H phase, where E_{rel} was calculated using DFT. Pink, blue, and green balls represent W, Mo, and Se atoms, respectively. The metal vacancies in the top and bottom layer are marked by the solid and dashed orange circles, respectively.

	2H WSe_2	2M WSe_2
[001]	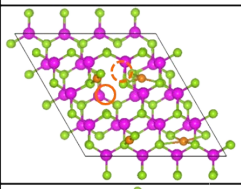	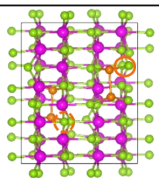
[010]	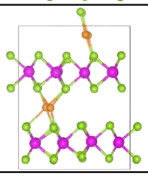	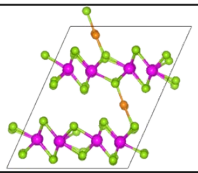
E_{rel}	0	29.296 meV

	2H $MoSe_2$	2M $MoSe_2$
[001]	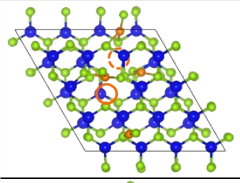	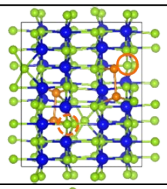
[010]	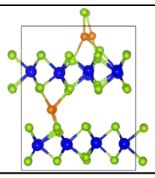	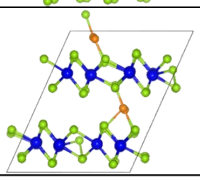
E_{rel}	0	50.214 meV

	$W_{0.75}Mo_{0.25}Se_2$			
	W vacancy		Mo vacancy	
	2H	2M	2H	2M
[001]	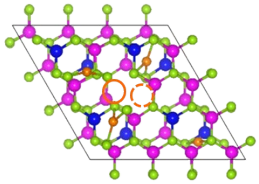	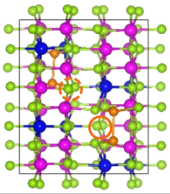	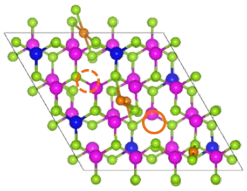	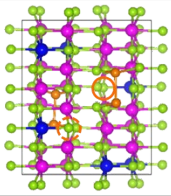
[010]	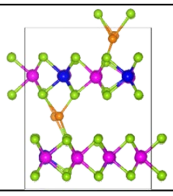	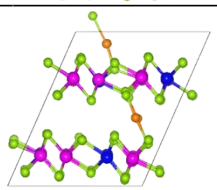	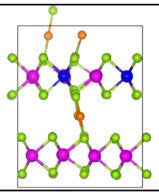	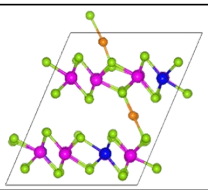
E_{rel}	0	40.000 meV	0	31.086 meV

	$W_{0.5}Mo_{0.5}Se_2$			
	W vacancy		Mo vacancy	
	2H	2M	2H	2M
[001]	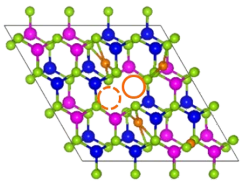	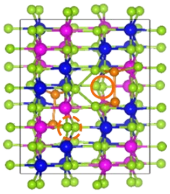	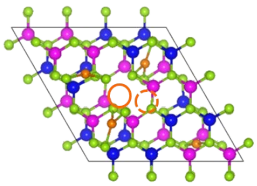	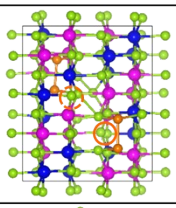
[010]	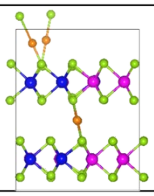	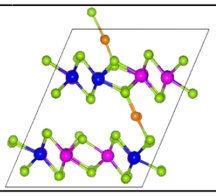	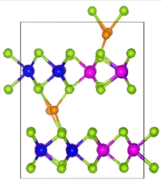	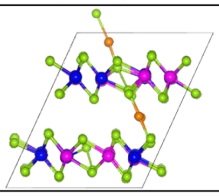
E_{rel}	0	46.357 meV	0	41.602 meV

	$W_{0.25}Mo_{0.75}Se_2$			
	W vacancy		Mo vacancy	
	2H	2M	2H	2M
[001]	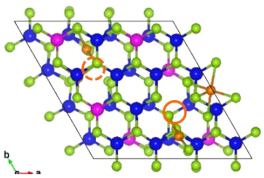	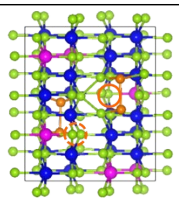	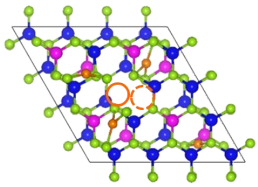	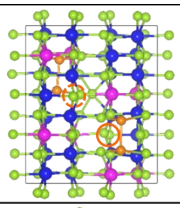
[010]	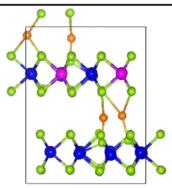	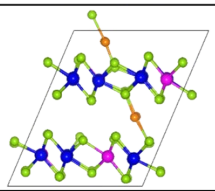	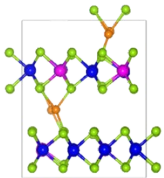	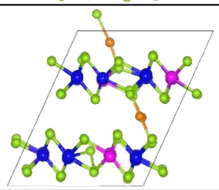
E_{rel}	0	41.665 meV	0	45.857 meV

Figure S8. Configurations for metal vacancy/Se intercalation combination (MV + I) model of 2H and 2M phase $W_{1-x}Mo_xSe_2$ at x = 0, 0.25, 0.5, 0.75, and 1, which were built from (4× 4 × 1) supercell with two layers. They were projected along [001] and [010]. The relative energy (E_{rel}) per atom is with respect to the most stable 2H phase, where E_{rel} was calculated using DFT. Pink, blue, and green balls represent W, Mo, and Se atoms, respectively. Orange balls correspond to the intercalated 4Se atoms. The metal vacancies in the top and bottom layer are marked by the solid and dashed orange circles, respectively.

(a)

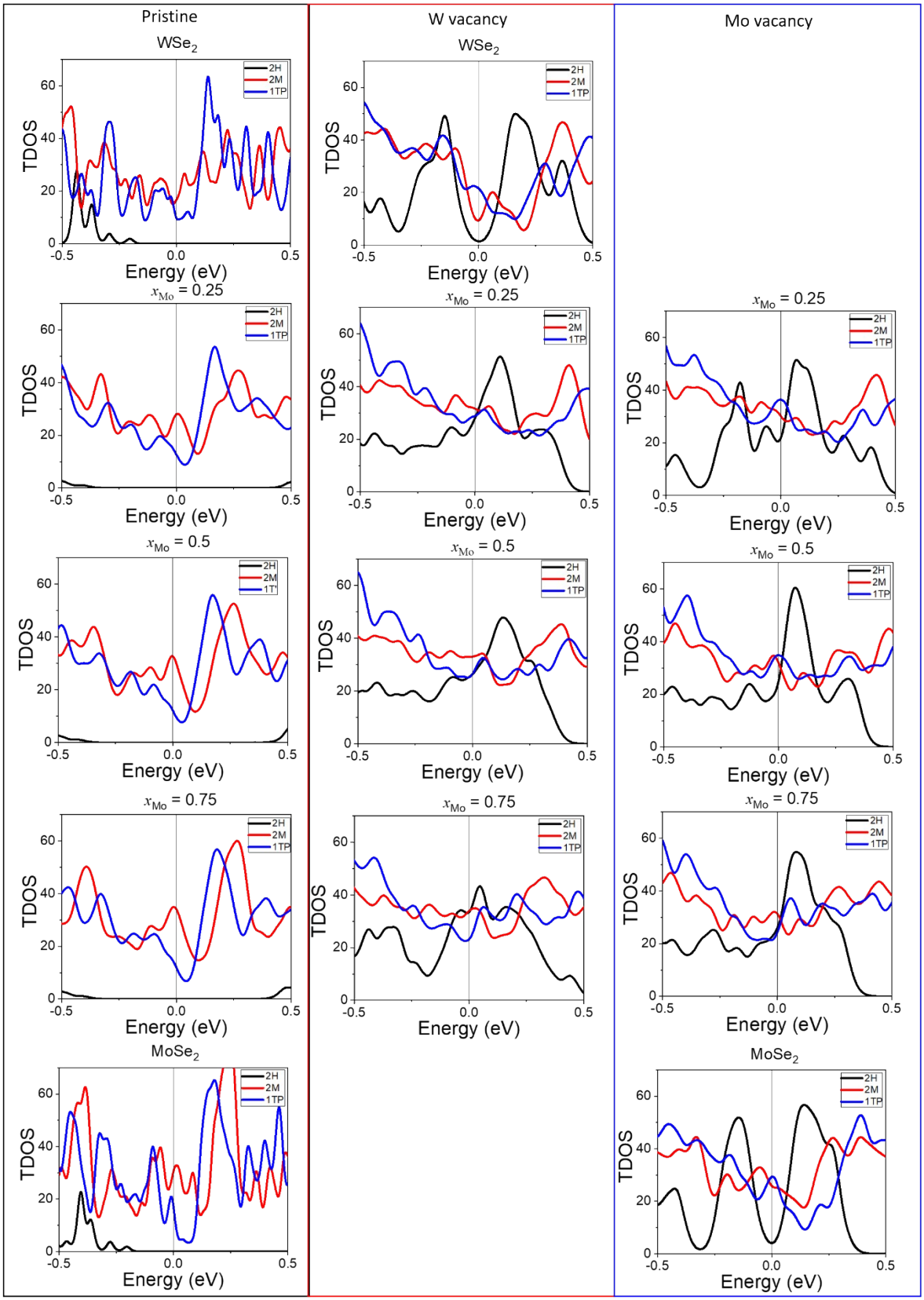
Pristine
W vacancy
Mo vacancy
WSe2
xMo = 0.25
xMo = 0.5
xMo = 0.75
MoSe2
TDOS
Energy (eV)
2H
2M
1TP

(b)

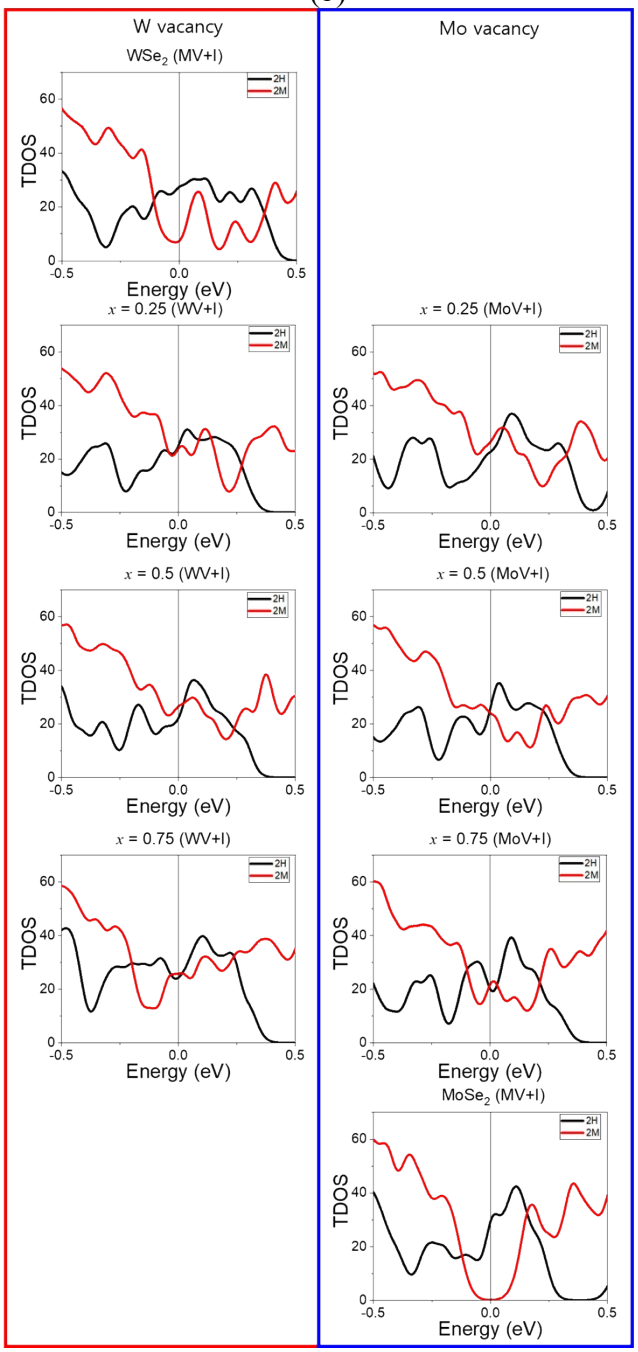

Figure S9. (a) TDOS of 2H, 2M, and 1T' (denoted as 1TP in the graph) phase $W_{1-x}Mo_xSe_2$ at x = 0, 0.25, 0.5, 0.75, and 1, in the pristine and metal (W and Mo) vacancy models, calculated using DFT (U_{eff} = 0). (b) TDOS of 2H and 2M phase $W_{1-x}Mo_xSe_2$ at x = 0, 0.25, 0.5, 0.75, and 1, in a combination model (MV + I) of metal (W and Mo) vacancy and Se intercalation, calculated using DFT (U_{eff} = 0). Fermi level is set to zero. The pristine 2H and 2M/1T' phases are semiconducting and metallic, respectively. As x increases to 0.25-1, the MV and MV + I models of 2M phase become more metallic because the DOS increases in the region of adjacent E_F.

(a)

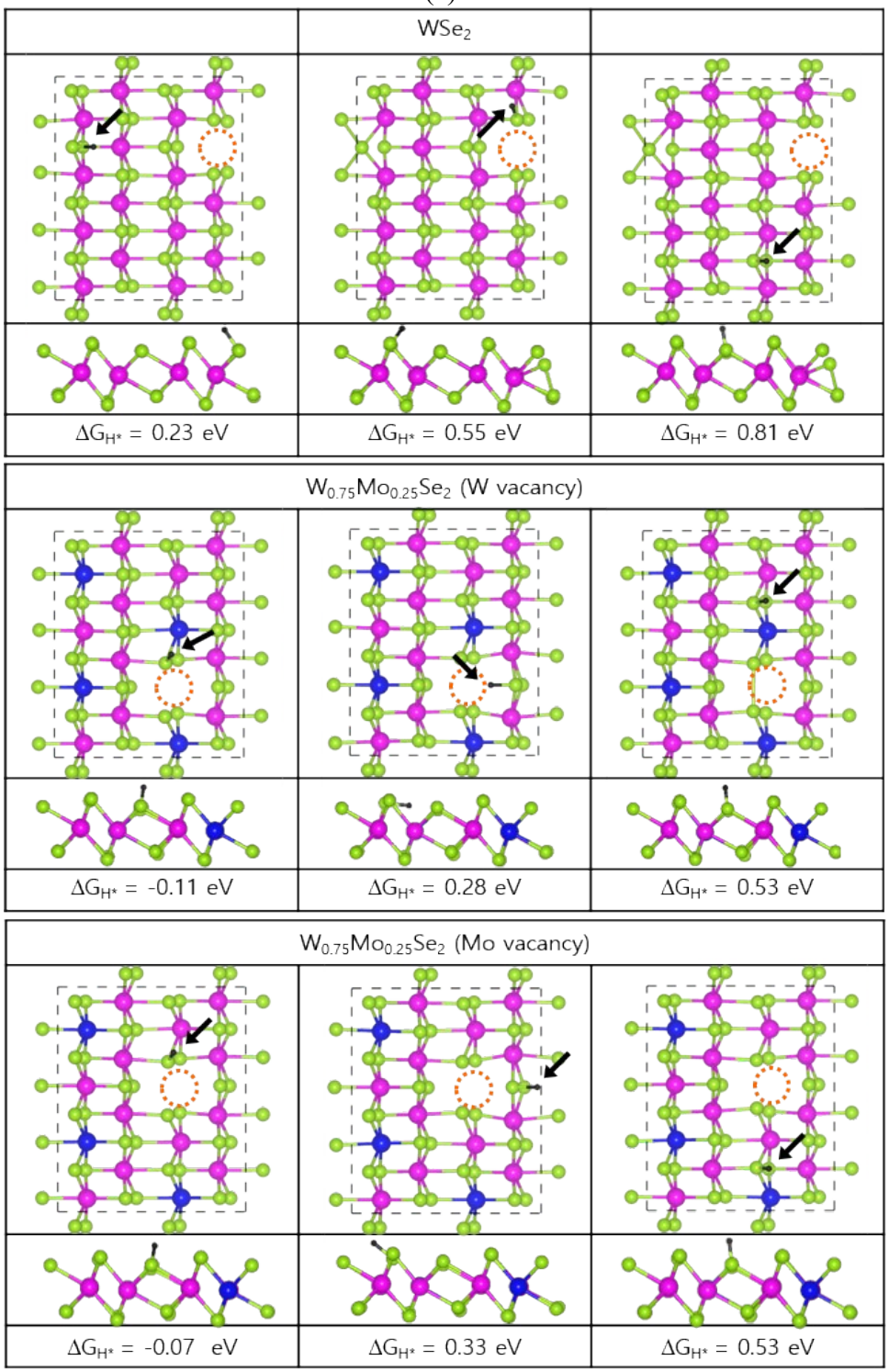
WSe2
ΔGH* = 0.23 eV
ΔGH* = 0.55 eV
ΔGH* = 0.81 eV
W0.75Mo0.25Se2 (W vacancy)
ΔGH* = -0.11 eV
ΔGH* = 0.28 eV
ΔGH* = 0.53 eV
W0.75Mo0.25Se2 (Mo vacancy)
ΔGH* = -0.07 eV
ΔGH* = 0.33 eV
ΔGH* = 0.53 eV

(b)

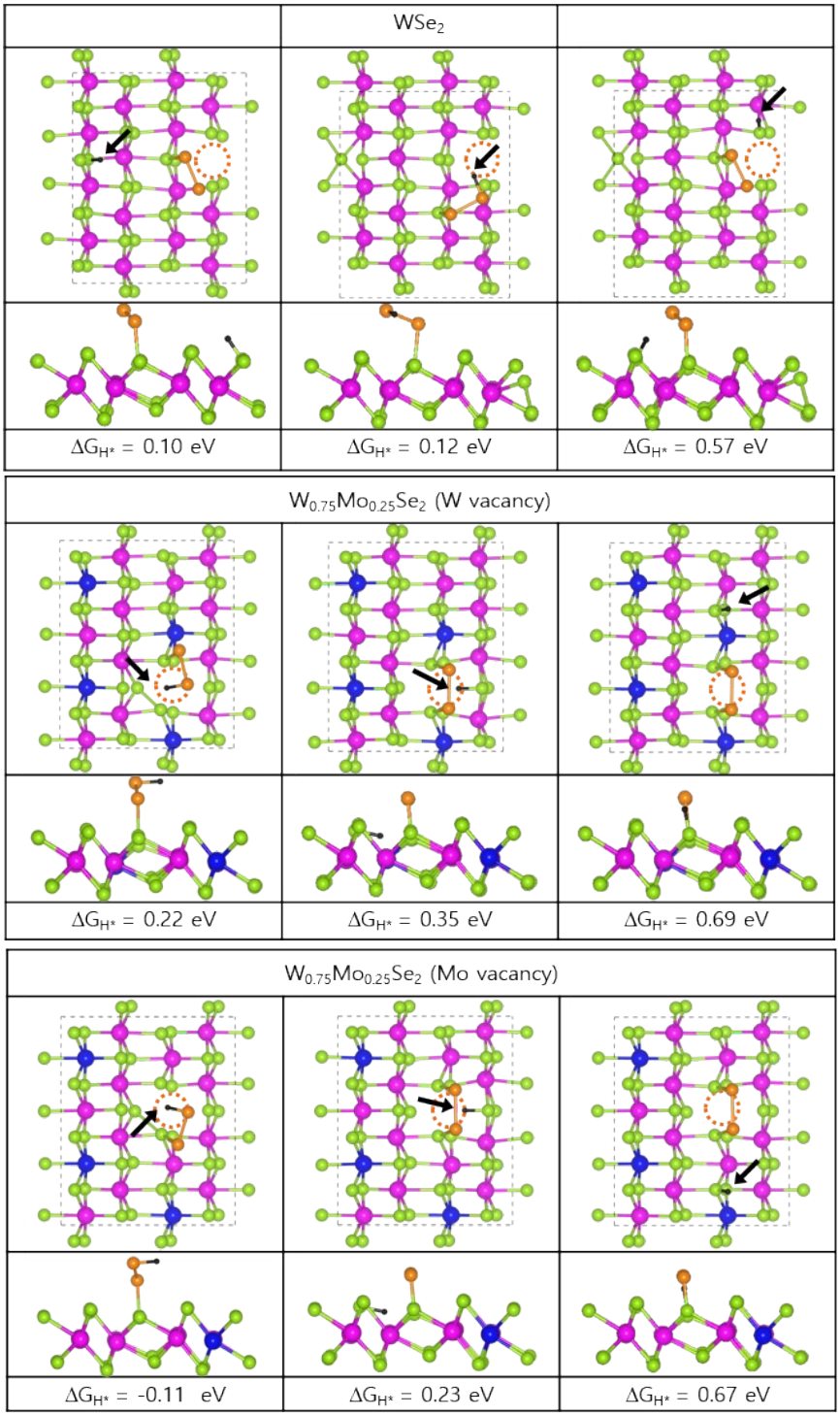

Figure S10. Crystal structures of the HER intermediates calculated using DFT. Various H adsorption sites in (a) the metal vacancy (MV) model and (b) metal vacancy/intercalation combination (MV + I) model of WSe_2 and $W_{0.75}Mo_{0.25}Se_2$. Configurations were chosen from the configurations shown in Figures S7 and S8. Gibbs free energy (ΔG_{H*}) is given for each site. Pink, blue, and green balls represent W, Mo, and Se atoms, respectively. Orange balls correspond to the Se adatoms. The metal vacancies are marked by the dashed orange circle. The small black ball (see arrows) represents the adsorbed H atom.

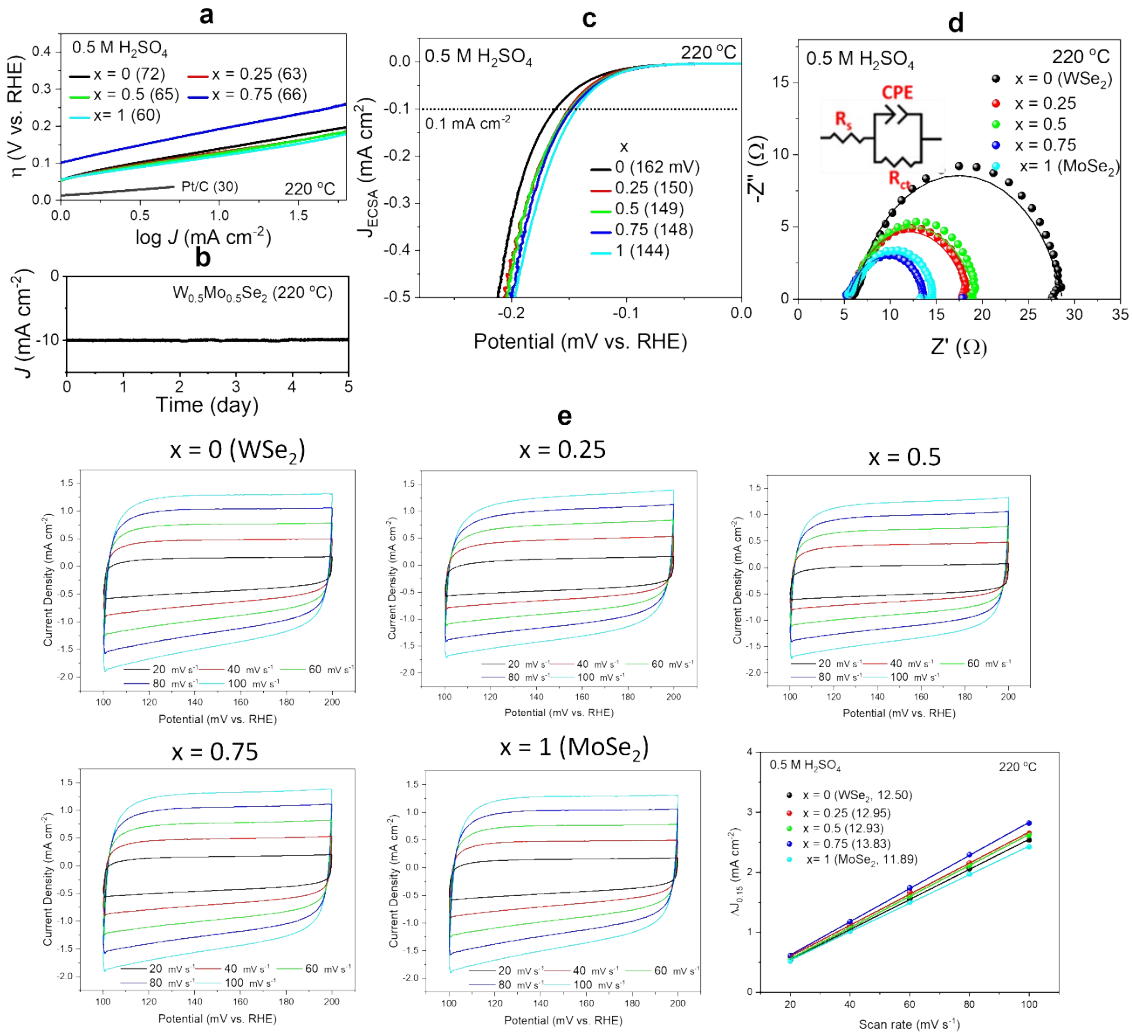

Figure S11. HER performance data of $W_{1-x}Mo_xSe_2$ samples (synthesized at 220 °C) in 0.5 M H_2SO_4. (a) Tafel plots, (b) chronoamperometric (CA) response of the x = 0.5 sample at $\eta_{J=10}$ (128 mV) for 5 days, and (c) electrochemically active surface area (ECSA)-normalized LSV curves. The value of parenthesis in Tafel and ECSA-normalized LSV represents Tafel slope (b) and $\eta_{JECSA=0.1}$, respectively. (d) Nyquist plots of $W_{1-x}Mo_xSe_2$ samples, using the frequency in the range from 100 kHz to 0.1 Hz at a potential of -0.15 V (η = 150 mV). The modified Randles circuit for fitting is shown in the inset. (d) Cyclic voltammetry (CV) curves of samples in a non-Faradaic region at 20-100 mV s^{-1} scan rates (with a step of 20 mV s^{-1}). The scan range is 0.1–0.2 V *vs.* RHE. Difference (ΔJ) between the anodic charging and cathodic discharging currents measured at 0.15 V *vs.* RHE and plotted as a function of the scan rate. The value in parenthesis represents the C_{dl}, obtained by the half of the linear slope.

(a) Tafel plots (η *vs.* log J) derived from the LSV curves (shown in Figure 5d), based on the equation $\eta = b \log(J/J_0)$, where b is the Tafel slope and J_0 is the exchange current density (extrapolated value at η = 0). Linear fit provides the b values (in parentheses).

(b) CA responses of the x = 0.5 sample at $\eta_{J=10}$ (128 mV) for 5 days shows negligible current attenuation (2%). The XRD, XPS, and EDX data confirm that the 2M phase persisted with the

same phase and composition (Figure S13).

(c) The electrochemically active surface area (ECSA) was defined as $C_{dl}/0.06$ (see Experimental Section in Supporting Information).

(d) Electrochemical impedance spectroscopy (EIS) measurements of the samples were performed using an amplitude of 10 mV. In the high-frequency limit and under non-Faradaic conditions, the electrochemical system is approximated by the modified Randles circuit shown in the inset, where R_s denotes the solution resistance, CPE is a constant-phase element related to the double-layer capacitance, and R_{ct} is the charge-transfer resistance from any residual Faradaic processes. A semicircle in the low-frequency region of the Nyquist plots represents the charge transfer process, with the diameter of the semicircle reflecting the charge-transfer resistance. The real (Z') and negative imaginary ($-Z''$) components of the impedance are plotted on the x and y axes, respectively. The simulation of the EIS spectra using an equivalent circuit model allowed us to determine the charge transfer resistance, R_{ct}, which is a key parameter for characterizing the catalyst-electrolyte charge transfer process. The fitting parameters are summarized as follows. A smaller R_{ct} implies more facile electron transfer kinetics that enhances the catalytic activity. Since R_{ct} decreases with x, where the best HER performance shows could be ascribed to the fastest electron transfer rate.

[Fitting Impedance parameters for the equivalent circuit]

Electrolyte	x	Rs (Ω)	CPE (mF)	R_{ct} (Ω)
0.5 M H_2SO_4	0	6.21	4.4	22.4
	0.25	5.65	5.3	12.7
	0.5	5.64	5.0	13.6
	0.75	3.68	5.8	11.1
	1	5.52	5.0	9.2

(e) For CV curves, the difference ($\Delta J_{0.15}$) between the anodic charging and cathodic discharging currents measured at 0.15 V (*vs.* RHE) was plotted as a function of scan rate. The slope of the straight line is equal to $2 \times C_{dl}$. The scan rates were 20–100 mV s^{-1}.

[C_{dl} values]

Electrolytes	x	C_{dl} (mF cm^{-2})
0.5 M H_2SO_4	0	12.50
	0.25	12.95
	0.5	12.93
	0.75	13.83
	1	11.89

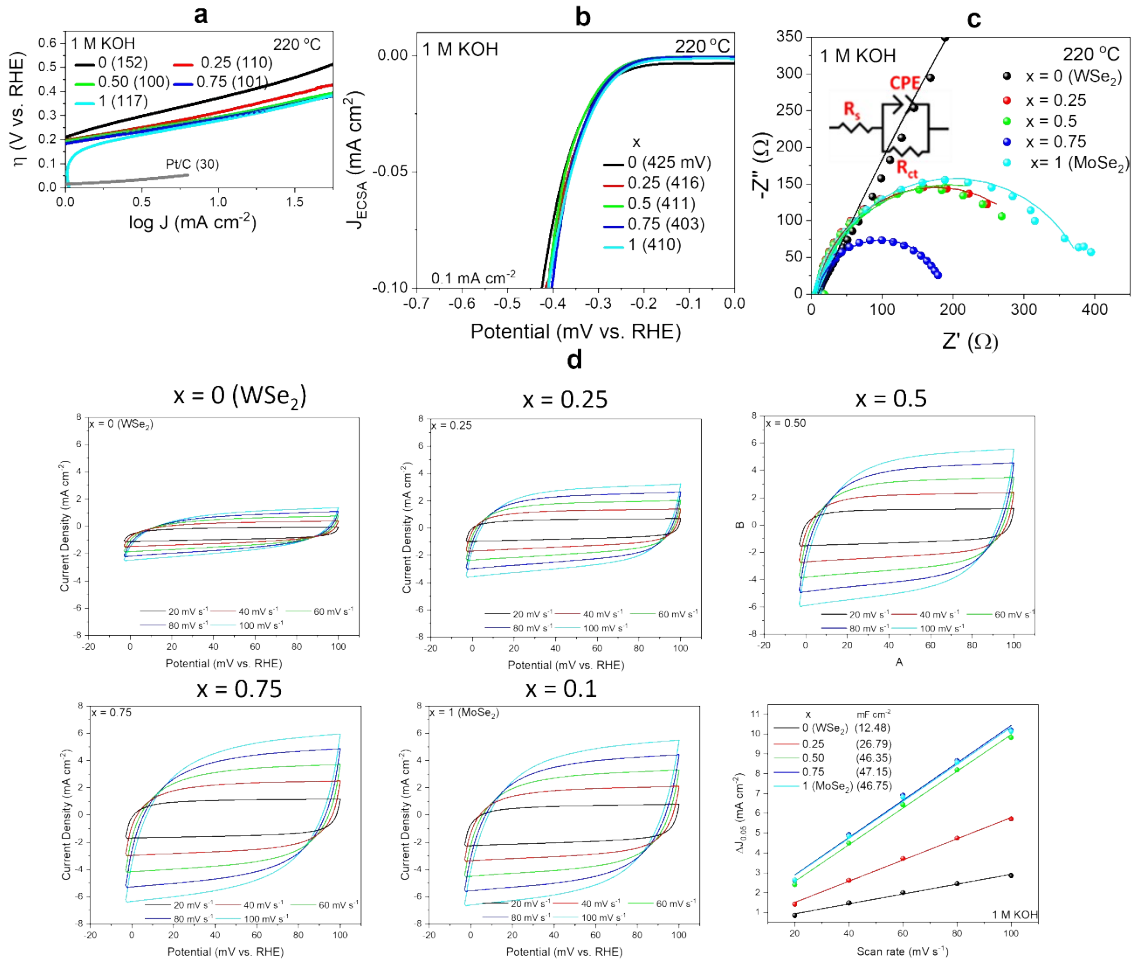

Figure S12. HER performance data for $W_{1-x}Mo_xSe_2$ (synthesized using r_P = 4 at 220 °C) in 1 M KOH. (a) Tafel plots, (b) electrochemically active surface area (ECSA)-normalized LSV curves. The value of parenthesis in the Tafel and ECSA-normalized LSV represents Tafel slope (*b*) and $\eta_{JECSA=0.1}$, respectively. (c) Nyquist plot using the frequency in the range from 100 kHz to 0.1 Hz at a potential of -0.15 V (η = 150 mV). The modified Randles circuit for fitting is shown in the inset. (d) Cyclic voltammetry (CV) curves of samples in a non-Faradaic region at 20-100 mV s^{-1} scan rates (with a step of 20 mV s^{-1}). The scan range is 0.1–0.2 V *vs.* RHE. Difference (Δ*J*) between the anodic charging and cathodic discharging currents measured at 0.15 V *vs.* RHE and plotted as a function of the scan rate. The value in parenthesis represents the C_{dl}, obtained by the half of the linear slope.

[Fitting Impedance parameters for the equivalent circuit]

Electrolyte	*x*	Rs (Ω)	CPE (mF)	R_{ct} (Ω)
1 M KOH	0	6.86	1.37	8273
	0.25	7.37	0.10	336
	0.5	6.62	0.10	374
	0.75	7.50	0.12	182
	1	7.25	0.52	387

For CV curves, the difference ($\Delta J_{0.15}$) between the anodic charging and cathodic discharging currents measured at 0.15 V (*vs.* RHE) was plotted as a function of scan rate. The slope of the straight line is equal to $2 \times C_{dl}$. The scan rates were 20−100 mV s^{-1}.

[C_{dl} values]

Electrolytes	x	C_{dl} (mF cm^{-2})
1 M KOH	0	12.48
	0.25	26.79
	0.5	46.36
	0.75	47.15
	1	46.75

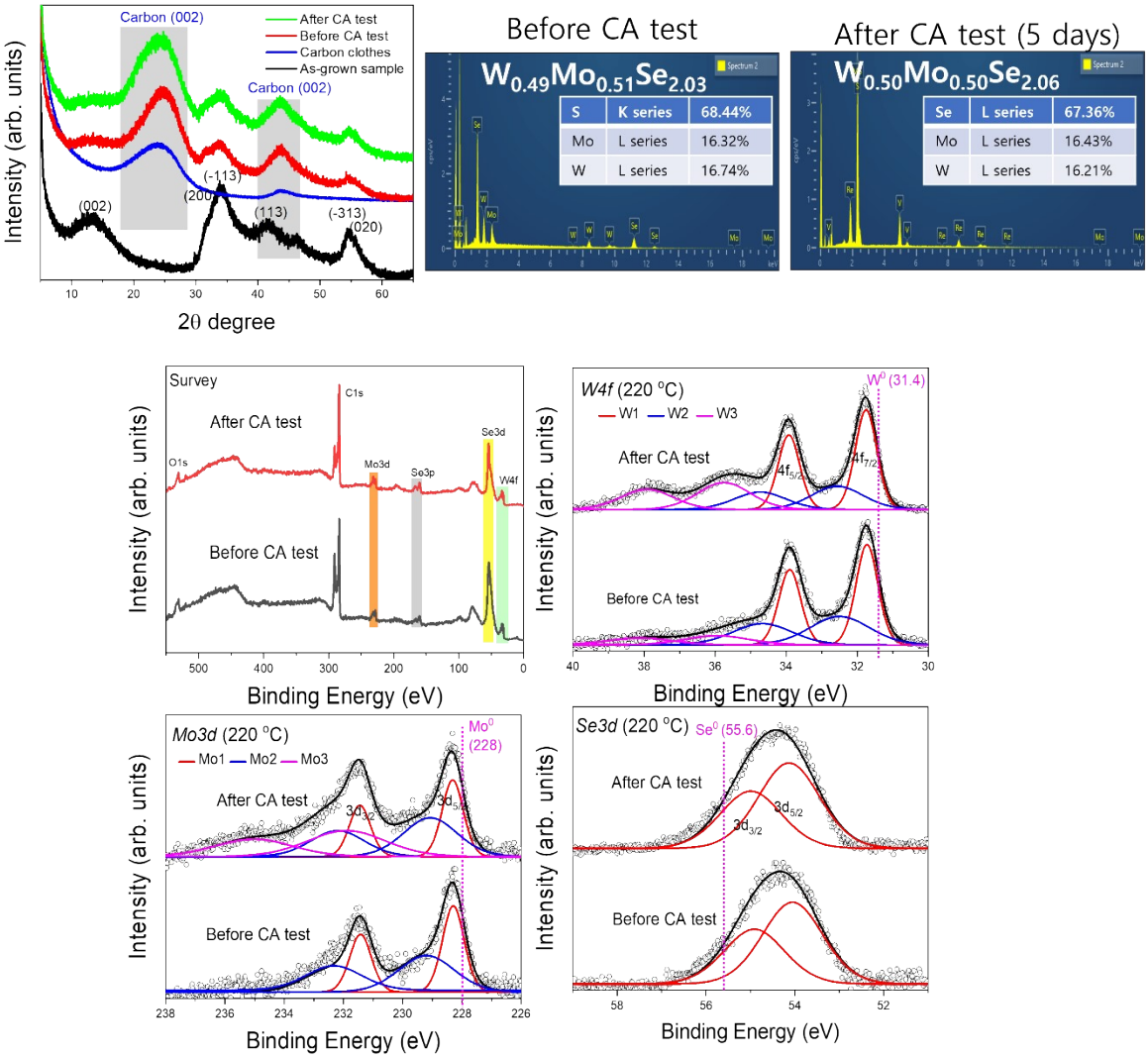

Figure S13. Characterization of $W_{0.5}Mo_{0.5}Se_2$ (synthesized using $r_P = 4$ at 220 °C and deposited on carbon cloth) before/after the 5-days CA test in 0.5 M H_2SO_4; XRD pattern, EDX, and XPS spectra after the CA test.

XRD patterns show that the 2M phase remains the same after CA test. There is not much change of Se abundance; $x = 2.03$ (before HER) and 2.06 (after HER). No Pt contamination of the after samples was confirmed in the EDX spectrum. The XPS also confirmed that no Pt deposition occurred, and the metallic properties of the samples remained during the HER. The experimental data (open circles) are fitted by a Voigt function, after the background correction with a Shirley-type baseline. After the CA test, the adsorption of electrolyte results in an increase of the higher-oxidation states (W3 and Mo3) for W and Mo, and Se. Nevertheless, the metallic properties remained. No Pt peak at 72.1 eV appeared after CA test.

References

(S1) Li, L.; Qin, Z.; Ries, L.; Hong, S.; Michel, T.; Yang, J.; Salameh, C.; Bechelany, M.; Miele, P.; Kaplan, M.; Chhowalla, M.; Voiry, D. Role of Sulfur Vacancies and Undercoordinated Mo Regions in MoS_2 Nanosheets toward the Evolution of Hydrogen. *ACS Nano* **2019**, *13*, 6824-6834.

(S2) Kresse, G.; Furthmüller, J. Efficient Iterative Schemes for *Ab initio* Total-Energy Calculations Using a Plane-Wave Basis Set. *Phys. Rev. B* **1996**, *54*, 11169-11186.

(S3) Kresse, G.; Furthmüller, J. Efficiency of *Ab initio* Total-Energy Calculations for Metals and Semiconductors Using a Plane-Wave Basis Set. *Comput. Mater. Sci.* **1996**, *6*, 15-50.

(S4) Blöchl, P. E. Projector augmented-wave method. *Phys. Rev. B*, **1994**, *50*, 17953-17979.

(S5) Grimme, S. Semiempirical GGA-type Density Functional Constructed with a Long-Range Dispersion Correction. *J. Comput. Chem*. **2006**, *27*, 1787-1799.

(S6) Grimme, S.; Antony, J.; Ehrlich S.; Krieg, H. A Consistent and Accurate ab initio Parametrization of Density Functional Dispersion Correction (DFT-D) for the 94 elements H-Pu. *J. Chem. Phys.* **2010**, *132*, 154104.

(S7) Tesch. R.; Kowalski P. M. Hubbard *U* Parameters for Transition Metals from First Principles. *Phys. Rev. B* **2022**, *105*, 195153.

(S8) Mou, J.; Gao, Y.; Wang, J.; Ma, J.; Ren, H. Hydrogen Evolution Reaction Activity Related to the Facet-Dependent Electrocatalytic Performance of NiCoP from First Principles. *RSC Advances* **2019**, *9*, 11755-11761.

(S9) Cramer C. J. *Essentials of Computational Chemistry: Theories and Models, 2nd Edition*; John Wiley & Sons Ltd.: West Sussex, **2004**; Chapter 10.

(S10) Voiry, D.; Yamaguchi, H.; Li, J.; Silva, R.; Alves, D. C. B.; Fujita, T.; Chen, M.; Asefa, T.; Shenoy, V. B.; Eda, G.; Chhowalla, M. Enhanced Catalytic Activity in Strained Chemically Exfoliated WS_2 Nanosheets for Hydrogen Evolution. *Nat. Mater.* **2013**, *12*, 850-855.

(S11) Chia, X.; Sutrisnoh, N. A. A.; Sofer, Z.; Luxa, J.; Pumera, M. Morphological Effects and Stabilization of the Metallic 1T Phase in Layered V-, Nb-, and Ta-Doped WSe_2 for Electrocatalysis. *Chem. Eur. J.* **2018**, *24*, 3199-3208.

(S12) Liu, Z.; Li, N.; Su, C.; Zhao, H.; Xu, L.; Yin, Z.; Li, J.; Du, Y. Colloidal Synthesis of 1T' Phase Dominated WS_2 Towards Endurable Electrocatalysis. *Nano Energy* **2018**, *50*, 176-181.

(S13) Jiang, A.; Zhang, B.; Li, Z.; Jin, G.; Hao, J. Vanadium-Doped WS_2 Nanosheets Grown on Carbon Cloth as a Highly Efficient Electrocatalyst for the Hydrogen Evolution Reaction. *Chem. Asian J.* **2018**, *13*, 1438-1446.

(S14) Shi, X.; Fields, M.; Park, J.; McEnaney, J. M.; Yan, H.; Zhang, Y.; Tsai, C.; Jaramillo, T. F.; Sinclair, R.; Nørskov, J. K.; Zheng, X. Rapid Flame Doping of Co to WS_2 for Efficient Hydrogen Evolution. *Energy Environ. Sci.* **2018**, *11*, 2270-2277.

(S15) Sokolikova, M. S.; Sherrell, P. C.; Palczynski, P.; Bemmer, V. L.; Mattevi, C. Direct Solution-Phase Synthesis of 1T' WSe_2 Nanosheets. *Nat. Commun.* **2019**, *10*, 712.

(S16) Kadam, S. R.; Enyashin, A. N.; Houben, L.; Bar-Ziv, R.; Bar-Sadan, M. Ni-WSe_2 Nanostructures as Efficient Catalysts for Electrochemical Hydrogen Evolution Reaction (HER) in Acidic and Alkaline Media. *J. Mater. Chem. A* **2020**, *8*, 1403-1416.

(S17) Han, A.; Zhou, X.; Wang, X.; Liu, S.; Xiong, Q.; Zhang, Q.; Gu, L.; Zhuang, Z.; Zhang, W.; Li, F.; Wang, D.; Li, L. J.; Li, Y. One-Step Synthesis of Single-Site Vanadium Substitution in 1T-WS_2 Monolayers for Enhanced Hydrogen Evolution Catalysis. *Nat. Commun.* **2021**, *12*, 709.

(S18) Zhang, W.; Liu, X.; Liu, T.; Chen, T.; Shen, X.; Ding, T.; Cao, L.; Wang, L. Luo, Q.; Yao, T. In Situ Investigation on Doping Effect in Co-Doped Tungsten Diselenide Nanosheets for Hydrogen Evolution Reaction. *J. Phys. Chem. C* **2021**, *125*, 6229-6236.

(S19) Muska, M.; Yang, J.; Sun, Y.; Wang, J.; Wang, Y.; Yang, Q. $CoSe_2$ Nanoparticles Dispersed in WSe_2 Nanosheets for Efficient Electrocatalysis and Supercapacitance Applications. *ACS Appl. Nano Mater.* **2021**, *4*, 5796-5807.

(S20) Liu, Z.; Nie, K.; Qu, X.; Li, X.; Li, B.; Yuan, Y.; Chong, S.; Liu, P.; Li, Y.; Yin, Z.; Huang, W. General Bottom-Up Colloidal Synthesis of Nano-Monolayer Transition-Metal Dichalcogenides with High 1T′-Phase Purity. *J. Am. Chem. Soc.* **2022**, *144*, 4863-4873.

(S21) Park, Y. J.; So, H. S.; Hwang, H.; Jeong, D. S.; Lee, H. J.; Lim, L.; Kim, C. G.; Shin, H. S. Synthesis of 1T WSe_2 on an Oxygen-Containing Substrate Using a Single Precursor. *ACS Nano* **2022**, *16*, 11059-11065.

(S22) Kwon, I. S.; Kwak, I. H.; Zewdie, G. M.; Lee, S. J.; Kim, J. Y.; Yoo, S. J.; Kim, J. -G.; Park, J.; Kang, H. S. WSe_2-VSe_2 Alloyed Nanosheets to Enhance the Catalytic Performance of Hydrogen Evolution Reaction. *ACS Nano* **2022**, *16*, 12569-12579.

(S23) Kwak, I. H.; Kwon, I. S.; Kim, J. Y.; Zewdie, G. M.; Lee, S. J.; Yoo, S. J.; Kim, J. -G.; Park, J.; Kang, H. S. Full Composition Tuning of $W_{1-x}Nb_xSe_2$ Alloy Nanosheets to Promote the Electrocatalytic Hydrogen Evolution Reaction. *ACS Nano* **2022**, *16*, 13949-13958.

(S24) Kwon, I. S.; Lee, S. J.; Kwak, I. H.; Zewdie, G. M.; Lee, S. J.; Yoo, S. J.; Kim, J. -G.; Park, J.; Kang, H. S. Composition-Tuned (MoWV)Se_2 Ternary Alloy Nanosheets as Excellent Hydrogen Evolution Reaction Electrocatalysts. *ACS Nano* **2023**, *17*, 2968-2079.

(S25) Zhao, Y.; Mao, G.; Du, Y.; Cheng, G.; Luo, W. Colloidal Synthesis of NiWSe Nanosheets for Efficient Electrocatalytic Hydrogen Evolution Reaction in Alkaline Media. *Chem. Asian J.* **2018**, *13*, 2040-2045.

(S26) Zhang, Y.; Shi, M.; Wang, C.; Zhu, Y.; Li, N.; Pu, X.; Yu, A.; Zhai, J. Vertically aligned NiS_2/CoS_2/MoS_2 Nanosheet Array as an Efficient and Low-Cost Electrocatalyst for Hydrogen Evolution Reaction in Alkaline Media. *Sci. Bull.* **2020**, *65*, 359- 366.

(S27) Kadam, S. R.; Enyashin, A. N.; Houben, L.; Bar-Ziv, R.; Bar-Sadan, M. Ni–WSe_2

Nanostructures as Efficient Catalysts for Electrochemical Hydrogen Evolution Reaction (HER) in Acidic and Alkaline Media. *J. Mater. Chem. A* **2020**, *8*, 1403-1416.

(S28) Yang, Y.; Zhao, X.; Mao, H.; Ning, R.; Zheng, X.; Sui, J.; Cai, W. Nickel-Doped $MoSe_2$ Nanosheets with Ni-Se Bond for Alkaline Electrocatalytic Hydrogen Evolution. *Int. J. Hydrog.Energy* **2020**, *45*, 10724-10728.

(S29) Kim, M.; Anjum, M. A. R.; Choi, M.; Jeong, H. Y.; Choi, S. H.; Park, N.; Lee, J. S. Covalent 0D–2D Heterostructuring of Co_9S_8–MoS_2 for Enhanced Hydrogen Evolution in All pH Electrolytes. *Adv. Funct. Mater.* **2020**, *30*, 2002536.

(S30) Tang, X.; Zhang, J.-Y.; Mei, B.; Zhang, X.; Liu, Y.; Wang, J.; Li, W. Synthesis of Hollow $CoSe_2$/$MoSe_2$ Nanospheres for Efficient Hydrazine Assisted Hydrogen Evolution. *Chem. Eng. J.* **2021**, *404*, 126529.

(S31) Inta, H. R.; Ghosh, S.; Mondal, A.; Tudu, G.; V S R M Koppisetti, H.; Mahalingam, V. $Ni_{0.85}Se$/$MoSe_2$ Interfacial Structure: An Efficient Electrocatalyst for Alkaline Hydrogen Evolution Reaction. *ACS Appl. Energy Mater.* **2021**, *4*, 2828-2837.

(S32) Guo, X.; Wu, T.; Zhao, S.; Fang, Y.; Xu, S.; Xie, M.; Huang, F. Re Modulation of Metallic Ultrathin 2M-WS_2 for Highly Efficient Hydrogen Evolution in Both Acidic and Alkaline Media. *ACS Appl. Energy Mater.* **2022**, *5*, 7674-7680.

(S33) Zhou, L.; Yang, C.; Zhu, W.; Li, R.; Pang, X Zhen, Y.; Wang, C.; Gao, L.; Fu, F.; Gao, Z.; Liang, Y. Boosting Alkaline Hydrogen Evolution Reaction via an Unexpected Dynamic Evolution of Molybdenum and Selenium on $MoSe_2$ Electrode. *Adv. Energy Mater.* **2022**, *12*, 2202367.

(S34) Huang, F.; Cao, S.; Feng, C.; Li, Y.; Liang, Y.; Li, X.; Mei, H.; Fan, W.; Xu, B.; Yuan, S.; Dai, F.; Lu, X.; Hu, S.; Sum, D. Polydopamine Bridging Strategy Enables Pseudomorphic Transformation of Multi-Component MOFs into Ultrasmall NiSe/WSe_2@NC Heterojunctions for Enhanced Alkaline Hydrogen Evolution *Appl. Catal. B* **2023**, *334*, 122769.

(S35) Yan, W.; Ma, H.; Zhao, X.; Zhang, Y.; Vishniakov, P.; Wang, X.; Zhong, X.; Hong, Z.; Maximov, M. Y.; Song, L.; Peng, S.; Li, L. P and Se Binary Vacancies and Heterostructures Modulated MoP/$MoSe_2$ Electrocatalysts for Improving Hydrogen Evolution and Coupling Electricity Generation. *Small* **2023**, *19*, 2208270.

(S36) Yu, X.; Li, Y.; Fang, T.; Gao, J.; Ma, Y. Interfacial and Electronic Modulation of W Bridging Heterostructure Between WS_2 and Cobalt-Based Compounds for Efficient Overall Water Splitting. *Small* **2024**, *20*, 2304512.

(S37) Hu, X.; Gao, Y.; Luo, X.; Xiong, J.; Chen, P.; Wang, B. Insight into the Intrinsic Activity of Various Transition Metal Sulfides for Efficient Hydrogen Evolution Reaction. *Nanoscale* **2024**, *16*, 4909-4918.

(S38) Zhang, T.; Ye, Q.; Han, Z.; Liu, Q.; Liu, Y.; Wu, D.; Fan, H. J. Biaxial Strain Induced OH Engineer for Accelerating Alkaline Hydrogen Evolution. *Nat. Commun.* **2024**, *15*, 6508.

(S39) Yap, F. M.; Loh, J. Y.; Ong, W. -J. Synergic Integration of Self-Supported 1T/2H-WS2 and Nitrogen Doped rGO on Carbon Cloth for pH-Universal Electrocatalytic Hydrogen

Evolution. *Nano Res.* **2024**, *17*, 1267-1280.

(S40) Duraisamya, P.; Mummoorthia, G.; Jayaramb, A.; Easwarana, S. K.; Mani, N. A Novel Method for Engineering Active Sites Through In-Situ and Chemical Deposition: Robust $Ni_3S_2/MoS_2/WS_2$ Heterostructures for Efficient Water Splitting in an Alkaline Medium. *Int. J. Hydrog. Energy* **204**, *92*, 186-198.

(S41) Lai, Z.; He, Q.; Tran, T. H.; Repaka, D. V. M.; Zhou, D. D.; Sun, Y.; Xi, S.; Li, Y.; Chaturvedi, A.; Tan, C.; Chen, B.; Nam, G. -H.; Li, B.; Ling, C.; Zhai, W.; Shi, Z.; Hu, D.; Sharma, V.; Hu, Z.; Chen, Y.; Zhang, Z.; Yu, Y.; Wang, X. R.; Ramanujan, R. V.; Ma, Y.; Hippalgaonkar, K.; Zhang, H. Metastable 1T′-Phase Group VIB Transition Metal Dichalcogenide Crystals. *Nat. Mater.* **2021**, *20*, 1113-1120.

(S42) Kwak, I. H.; Kwon, I. S.; Debela, T. T.; Abbas, H. G.; Park, Y. C.; Ahn, J. P.; Park, J.; Kang, H. S. Se-Rich $MoSe_2$ Nanosheets and Their Superior Electrocatalytic Performance for Hydrogen Evolution Reaction. *ACS Nano* **2020**, *14*, 6295-6304.